

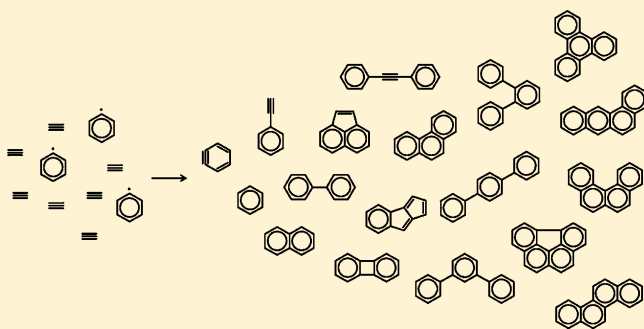
# Chemistry of Polycyclic Aromatic Hydrocarbons Formation from Phenyl Radical Pyrolysis and Reaction of Phenyl and Acetylene

A. Comandini, T. Malewicki, and K. Brezinsky\*

Department of Mechanical Engineering, University of Illinois at Chicago, 842 West Taylor Street, Chicago, Illinois 60607, United States

## S Supporting Information

**ABSTRACT:** An experimental investigation of phenyl radical pyrolysis and the phenyl radical + acetylene reaction has been performed to clarify the role of different reaction mechanisms involved in the formation and growth of polycyclic aromatic hydrocarbons (PAHs) serving as precursors for soot formation. Experiments were conducted using GC/GC-MS diagnostics coupled to the high-pressure single-pulse shock tube present at the University of Illinois at Chicago. For the first time, comprehensive speciation of the major stable products, including small hydrocarbons and large PAH intermediates, was obtained over a wide range of pressures (25–60 atm) and temperatures (900–1800 K) which encompass the typical conditions in modern combustion devices. The experimental results were used to validate a comprehensive chemical kinetic model which provides relevant information on the chemistry associated with the formation of PAH compounds. In particular, the modeling results indicate that the *o*-benzyne chemistry is a key factor in the formation of multi-ring intermediates in phenyl radical pyrolysis. On the other hand, the PAHs from the phenyl + acetylene reaction are formed mainly through recombination between single-ring aromatics and through the hydrogen abstraction/acetylene addition mechanism. Polymerization is the common dominant process at high temperature conditions.



## 1. INTRODUCTION

The development of chemical kinetic models able to accurately predict the formation of soot in combustion engines and turbines is strictly related to the accuracy in the description of the chemical mechanisms involved in the formation and growth of the polycyclic aromatic hydrocarbons (PAHs). Although several growth mechanisms have been proposed throughout the years, the multi-ring aromatic chemistry is far from being fully understood. The well-known hydrogen abstraction/acetylene addition (HACA) mechanism<sup>1,2</sup> is generally considered the principal pathway for the formation of large PAH compounds. The simplest system for which the HACA mechanism applies involves the reaction between phenyl radical and acetylene to form phenylacetylene and a subsequent additional HACA step which leads to the formation of the second-ring species.

Among the competing pathways, the reactions between aromatic radicals and aromatic molecules have been proposed in the past as efficient pathways for PAHs growth. Gordon et al.,<sup>3</sup> in their study on the chemistry of diffusion flames, reported the higher soot tendency of the benzene flames compared to the methane flames regardless of the similarity in acetylene concentrations. The authors hypothesized that the reaction between the biphenyl radical ( $C_{12}H_9$ ) and benzene could be responsible for the formation of large four-ring compounds, such as triphenylene, and subsequently of soot. The efficiency of the biphenyl route was subsequently demonstrated by

Frenklach et al. in their numerous pioneering studies on PAHs growth and soot formation.<sup>4–6</sup> As summarized in ref 6, Frenklach concluded that in general two competing growth pathways are present, one via HACA<sup>1,2</sup> and the other via aromatic–aliphatic linked hydrocarbons. Other authors have demonstrated how the addition of the phenyl radical and benzene to PAH molecules leads to the formation of larger fused-ring structures.<sup>7,8</sup> These addition processes can be considered as the prototype for the growth mechanism called reactive coagulation.<sup>9–12</sup> Reactive coagulation has been shown to be an efficient pathway to the formation of large PAHs through reaction between aromatic radicals and aromatic molecules, accompanied by hydrogen abstraction and cyclization. This idea has been recently proposed again by Shukla and Koshi.<sup>13,14</sup> In order to explain their experimental results on the pyrolysis of benzene, the authors hypothesized the so-called phenyl addition/cyclization mechanism (PAC). In this case, subsequent additions of phenyl radicals to aromatic molecules followed by cyclization lead to the formation of large intermediates.

A comprehensive study on the phenyl + acetylene reaction and on the phenyl radical pyrolysis would clearly lead to a

Received: August 4, 2011

Revised: February 15, 2012

Published: February 16, 2012



better understanding of the mechanisms involved in the formation of the primary PAH compounds which serve as building blocks for soot. The radical–radical recombination between phenyl radicals has been studied in the past as main source of biphenyl,<sup>15,16</sup> one of the most important intermediates for PAHs growth. In a recent paper, Tranter et al.<sup>17</sup> revisited the self-reaction of phenyl radicals based on low-pressure shock tube experiments and high-level theoretical calculations. The authors developed a chemical kinetic model which accurately simulates the laser schlieren experimental results. Nevertheless, the model does not include a complete mechanistic description of the PAHs formation which is expected to be relevant at the high pressure conditions present in typical modern combustion devices. Several experimental and numerical studies have also been performed on the phenyl + acetylene reaction.<sup>15,18–22</sup> However, to the best of our knowledge, there are no experimental investigations which provide a comprehensive speciation analysis of the products of the title reaction, including measurement of the large PAH compounds.

In order to better clarify the chemical mechanisms relevant for the formation of PAH compounds from the reactions involving the phenyl radical, both the phenyl radical pyrolysis and the pyrolytic reactions of the phenyl radical with acetylene were studied using the University of Illinois at Chicago high-pressure shock tube. Species profiles for all the major products, including light hydrocarbons and large polycyclic aromatic compounds, were produced and used to validate a comprehensive chemical kinetic model which helped improve the understanding of the title reactions.

## 2. EXPERIMENTAL APPARATUS

The single-pulse high-pressure shock tube (HPST) present at the University of Illinois at Chicago is a well characterized experimental device for identification and measurement of the stable reaction products behind reflected shock waves. The apparatus has been described in detail elsewhere,<sup>23,24</sup> and only the relevant features are reported here.

The HPST consists of a 117 in. long driven section of 1 in. i.d. and a driver section of 2 in. i.d. separated by a diaphragm section. The length of the driver section is varied by inserting metallic plugs in order to obtain constant reaction conditions as well as fast cooling of the reaction by the rarefaction wave. The typical driver section length varies between 40 and 60 in. A dump tank placed just ahead of the diaphragm section on the driven side rapidly quenches the reflected shock wave, thereby permitting the shock tube to be operated in single pulse fashion. The apparatus is heated to 100 °C.

The driven section is equipped with a set of seven high-frequency PCB piezoelectric pressure transducers, six positioned along the driven section and one located at the end-wall perpendicularly to the flow. The pressure profiles from the six pressure transducers are used to obtain the incident shock wave velocities extrapolated to the end-wall with an uncertainty  $\leq 1\%$ . Such velocities are experimentally related to the temperatures in the post-shock reaction by means of chemical thermometers.<sup>24</sup> The error associated with the shock-wave attenuation is minimized by the fact that the attenuation observed in the experiments is similar to the attenuation in the chemical thermometer calibration experiments conducted at similar temperature and pressure conditions. Three chemical thermometers were used in the present investigation: cyclopropanecarbonitrile<sup>25</sup> combined with 1,1,1-trifluoroethane<sup>26</sup>

for the temperature range below 1362 K, and carbon disulfide<sup>27</sup> for temperatures between 1691 and 2000 K. An interpolated calibration curve was used between 1362 and 1691 K. The estimated error in the post-shock temperature is around 1% for temperatures up to 1350 K, and 2% for temperatures higher than 1350 K. The pressure is measured directly from the pressure trace of the end-wall transducer while the reaction time is considered as the time between the arrival of the incident wave at the end-wall and the time when the pressure reaches the 80% of its maximum value.<sup>28</sup> Uncertainty in the time measurement is no more than 10%.

Reagent mixtures consisting of phenyl iodide and acetylene, if any, diluted in argon (ultrahigh purity grade, 99.999%) were prepared manometrically in 42 L vessels heated to 100 °C and allowed to stand overnight before use. Phenyl iodide (Aldrich 98%) was degassed several times using a freeze/thaw procedure prior to use, while acetylene (BOC, grade 2.6) was purified using a Balston 95A filter. Neon was added as an internal standard to account for any dilution by the driver gas (helium). Preliminary experiments on the phenyl iodide pyrolysis indicated that, 3 days after their preparation, the gas-phase mixtures could degrade, depending on the mole fraction of the reagent in the mixture. The observed decrease in the phenyl iodide mole fractions can be attributed to adsorption on the walls of the 42 L heated vessels. To avoid such problem, all the experimental sets presented in this work were conducted in a limited time frame, specifically within 2 days after the preparation of the gas-phase mixtures. In addition, for each experimental set the composition of the gas-phase mixture was periodically verified by GC analysis of samples obtained at low temperatures when no reaction products would be detected.

A sample of gas is withdrawn from the post-shock mixture through an automated sampling apparatus for subsequent analysis. A GC/GC-MS analytical system is connected directly to the end of the driven section through an electropolished stainless steel line treated for inertness and heated to 150 °C to avoid condensations. The analytical system consists of two Hewlett-Packard 6890 series gas chromatographs placed in series, the first equipped with two FID detectors connected to DB-17ms columns for calibration and measurement of heavy compounds, and the second equipped with a FID detector and a TCD detector connected respectively to a HP-PLOT Q column for measurement of light species and to a HP-PLOT MoleSieve column for measurement of inert compounds. A 5973 series mass spectrometer is also connected to the second GC for identification of unknown compounds in the mixtures.

The GC calibration for the relatively light hydrocarbons (up to naphthalene, included) was mainly performed using certified gas mixtures as well as in-house prepared calibration mixtures. Typical errors in the measurement of such species are around 5–10%. On the other hand, the uncertainty associated to the measurement of larger PAH compounds is expected to be higher due to the uncertainty in the corresponding gas-phase calibration curves. These calibration curves were deduced from the gas-phase calibration curve for naphthalene based on the relative ratio between the corresponding liquid-phase calibration curves. The liquid-phase calibration curves were obtained using certified solutions of PAHs in appropriate solvents. Very similar results were deduced using benzene instead of naphthalene as a reference compound. The maximum uncertainty in the measurement of C12 hydrocarbons is estimated as 15–20%, while for C14 compounds as 20–25%. For even larger compounds (terphenyls and four-ring species)

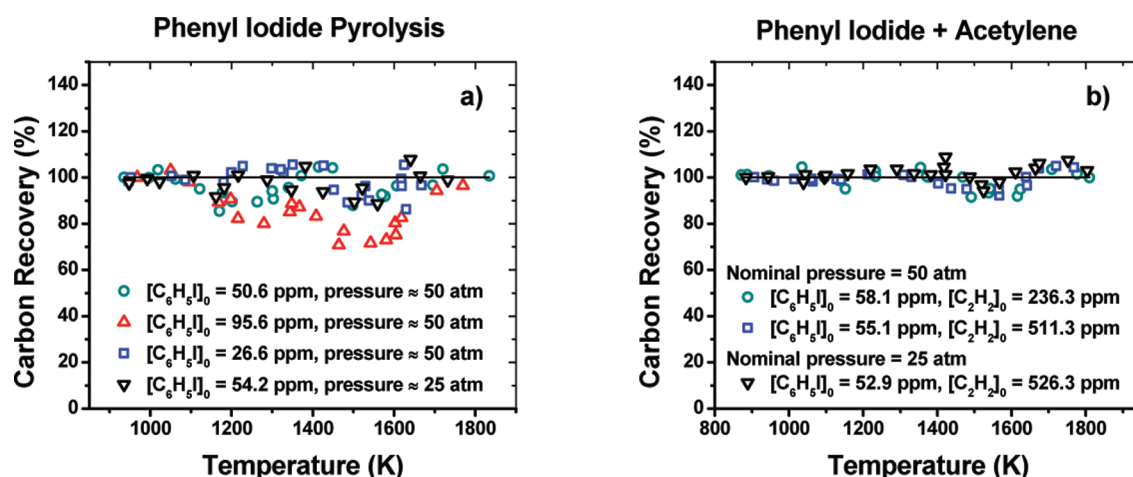


Figure 1. Experimental carbon balance: (a) phenyl iodide decomposition and (b) phenyl + acetylene reaction.

the uncertainty could be as high as a factor of 2 due to the large difference between the molecular weights of such compounds and the one of the reference species, naphthalene. The calibration curves for PAH compounds not present in the certified solutions were estimated on the basis of the calibration of similar compounds. Finally, calibration curves for diacetylene and triacetylene were deduced from experiments on acetylene decomposition (around 120 ppm in argon). Based on the fact that the calibration for acetylene is well known from standard calibration mixtures, the calibration for diacetylene was obtained from the experiments where only acetylene and diacetylene were detected as major species. Similarly, the calibration for triacetylene was deduced from the experiments where acetylene, diacetylene, and triacetylene were the only major detected products.

### 3. RESULTS AND DISCUSSION

In order to fully analyze the reaction systems in consideration, several experimental sets were obtained by varying both the initial concentrations of the reactants and the nominal pressure. First, the phenyl iodide decomposition has been investigated as a source of phenyl radicals for the subsequent experiments on the phenyl + acetylene reaction. Three experimental sets were conducted at a nominal pressure of 50 atm and initial phenyl iodide mole fractions of  $\sim 25$ , 50, and 100 ppm. One additional data set at 25 atm with  $\sim 50$  ppm of reactant in the initial mixture was carried out to test possible pressure effects. The carbon balance for most of the experimental sets presents a maximum error of  $\sim 10\%$ , as shown in Figure 1a, which indicates efficient recovery of all the reaction products as well as reliability of the GC calibration curves. The only exception is constituted by the data set obtained using an initial phenyl iodide mole fraction of 100 ppm, for which the carbon balance drops to 75% in the high-temperature range. In this case the relatively large  $C_6H_5I$  concentration leads to the formation of significant quantities of PAH intermediates. These intermediates could subsequently undergo processes such as aggregation or dimerization which lead to the formation of heavier PAHs and soot that cannot be measured by our gas-phase GC technique.

Subsequent experimental work has been conducted in order to study the phenyl + acetylene reaction. In this case three experimental sets were obtained by varying the initial acetylene mole fraction from  $\sim 250$  to 500 ppm with an initial phenyl

iodide concentration of  $\sim 50$  ppm. The carbon balance, as for the case of phenyl pyrolysis, indicates good recovery of the product species for all the data sets (Figure 1b).

A chemical kinetic model was developed to simulate the high-pressure experimental data on both the phenyl pyrolysis and the phenyl + acetylene reaction. Both the CHEMKIN 3.6.2<sup>29</sup> and the CHEMKIN 4.1.1<sup>30</sup> suites of programs were used to implement the model. For the modeling calculations, the exact reaction time, temperature, and pressure were specified for each shock along with the initial mole fractions of the reactants. The simulations were performed assuming an adiabatic constant pressure process. As discussed in our previous publication addressing this issue,<sup>28</sup> the adiabatic constant pressure process assumption leads to reasonable accuracy in predicting the stable species profiles.

The main reactions relevant to the formation and consumption of PAH compounds with associated reaction rate parameters are reported in Table 1. The thermochemical parameters for the species in the model were mainly taken from Burcat and Ruscic<sup>31</sup> and from chemical kinetic models available in the literature.<sup>32,33</sup> The thermochemical parameters not available in literature were estimated using the FITDAT utility from the CHEMKIN 3.7.1 collection.<sup>34</sup> FITDAT utilizes a least-squares fitting of the thermodynamic data in order to generate the polynomial coefficients in the format required by CHEMKIN. The FITDAT input file contains the species enthalpy and entropy at 298.15 K as well as the vibrational frequencies, which are used to estimate the thermodynamic properties as functions of the temperature. The enthalpies of the compounds, if not available on the NIST database, were calculated using the ring-conserved isodesmic reaction scheme.<sup>35</sup> The relative geometry optimizations and vibrational analyses were performed using the uB3LYP hybrid functional<sup>36,37</sup> with the Pople's valence triple- $\zeta$  basis set 6-311+G(d,p).<sup>38</sup> For species containing iodine atoms, i.e., the iodobiphenyls, the DGDZVP basis set<sup>39</sup> was used. All of the calculations were carried out with the Gaussian 03 program package.<sup>40</sup>

In the following paragraphs the relevant results from the experimental work and from the modeling simulations will be discussed for both the phenyl pyrolysis and the phenyl + acetylene reaction. In order to facilitate the discussion, the molecular structures of the major PAH products analyzed in this work are reported in Figure 2. All the experimental results

Table 1. Chemical Kinetic Model, Relevant Reactions, and Associated Reaction Rate Parameters

	reaction	A	n	E <sub>a</sub>	ref
Halogenated Compounds					
R1	$C_6H_5I \rightarrow C_6H_5 + I$	$1.374 \times 10^{15}$	0.00	64406	42
R2	$C_6H_5 + I \rightarrow C_6H_5I$	$1.00 \times 10^{13}$	0.00	0	est., see text
R3	$C_6H_5I \leftrightarrow o-C_6H_4 + HI$	$8.24 \times 10^{13}$	0.00	64406	see text
R4	$C_6H_5I + H \leftrightarrow C_6H_5 + HI$	$8.73 \times 10^5$	2.35	-37.3	81 <sup>a</sup>
R5	$C_6H_5 + HI \leftrightarrow C_6H_6 + I$	$3.00 \times 10^{12}$	0.00	0	est., see text
R6	$C_6H_5I + C_6H_5 \leftrightarrow C_{12}H_{10} + I$	$2.00 \times 10^{12}$	0.00	11000	46
R7	$C_6H_5I + C_6H_5 \leftrightarrow o-C_{12}H_9I + H$	$3.183 \times 10^{11}$	0.00	4305	see text
R8	$C_6H_5I + C_6H_5 \leftrightarrow m-C_{12}H_9I + H$	$3.183 \times 10^{11}$	0.00	4305	see text
R9	$C_6H_5I + C_6H_5 \leftrightarrow p-C_{12}H_9I + H$	$1.592 \times 10^{11}$	0.00	4305	see text
R10	$o-C_{12}H_9 + I \rightarrow o-C_{12}H_9I$	$1.00 \times 10^{13}$	0.00	0	est.
R11	$m-C_{12}H_9 + I \rightarrow m-C_{12}H_9I$	$1.00 \times 10^{13}$	0.00	0	est.
R12	$p-C_{12}H_9 + I \rightarrow p-C_{12}H_9I$	$1.00 \times 10^{13}$	0.00	0	est.
R13	$o-C_{12}H_9I \rightarrow o-C_{12}H_9 + I$	$1.374 \times 10^{15}$	0.00	64406	see text
R14	$m-C_{12}H_9I \rightarrow m-C_{12}H_9 + I$	$1.374 \times 10^{15}$	0.00	64406	see text
R15	$p-C_{12}H_9I \rightarrow p-C_{12}H_9 + I$	$1.374 \times 10^{15}$	0.00	64406	see text
R18	$I + H + AR \leftrightarrow HI + AR$	$2.00 \times 10^{21}$	-1.87	0	52
R19	$H + HI \leftrightarrow H_2 + I$	$3.98 \times 10^{13}$	0.00	0	46
Biphenyl and Benzene					
R20	$C_6H_5 + C_6H_5 \leftrightarrow C_{12}H_{10}$	$3.09 \times 10^{12}$	0.036	-1702	17, see text
R21	$C_6H_5 + C_6H_5 \leftrightarrow o-C_6H_4 + C_6H_6$	$8.52 \times 10^{-4}$	4.57	-5735	17, see text
R22	$C_6H_5 + C_6H_5 \leftrightarrow m-C_6H_4 + C_6H_6$	$8.52 \times 10^{-4}$	4.57	-5735	17, see text
R23	$C_6H_5 + C_6H_5 \leftrightarrow p-C_6H_4 + C_6H_6$	$4.26 \times 10^{-4}$	4.57	-5735	17, see text
R24	$o-C_6H_4 \leftrightarrow m-C_6H_4$	$2.12 \times 10^{14}$	0.00	73489.5	45
R25	$m-C_6H_4 \leftrightarrow p-C_6H_4$	$2.83 \times 10^{14}$	0.00	63045.7	45
R26	$p-C_6H_4 \leftrightarrow z-C_6H_4$	$1.00 \times 10^{13}$	0.00	17800	see text
R27	$o-C_6H_4 + C_6H_5 \leftrightarrow o-C_{12}H_9$	$1.00 \times 10^{13}$	0.00	3720	see text
R28	$m-C_6H_4 + C_6H_5 \rightarrow m-C_{12}H_9$	$1.00 \times 10^{13}$	0.00	3720	see text
R29	$p-C_6H_4 + C_6H_5 \rightarrow p-C_{12}H_9$	$1.00 \times 10^{13}$	0.00	3720	see text
R30	$m-C_{12}H_9 \rightarrow m-C_6H_4 + C_6H_5$	$2.223 \times 10^{15}$	0.00	87232	see text
R31	$p-C_{12}H_9 \rightarrow p-C_6H_4 + C_6H_5$	$2.223 \times 10^{15}$	0.00	87232	see text
R35	$o-C_{12}H_9 + H \leftrightarrow C_{12}H_{10}$	$4.27 \times 10^{13}$	0.338	-158	17
R36	$m-C_{12}H_9 + H \leftrightarrow C_{12}H_{10}$	$1.25 \times 10^{13}$	0.284	-155	17
R37	$p-C_{12}H_9 + H \leftrightarrow C_{12}H_{10}$	$2.78 \times 10^{13}$	0.185	15.3	17
R38	$C_6H_5 + C_6H_6 \leftrightarrow C_{12}H_{10} + H$	$9.55 \times 10^{11}$	0.00	4305	49
R44	$C_6H_5 + H(+M) \leftrightarrow C_6H_6(+M)$	$1.00 \times 10^{14}$	0.00	0	48 <sup>b</sup>
R45	$C_6H_6 + H \leftrightarrow C_6H_5 + H_2$	$4.00 \times 10^{15}$	0.00	20776	75 (x2)
Terphenyls and Triphenylene					
R46	$C_{12}H_{10} + C_6H_5 \leftrightarrow o\text{-TERPH} + H$	$6.367 \times 10^{11}$	0.00	4305	see text
R47	$C_{12}H_{10} + C_6H_5 \leftrightarrow m\text{-TERPH} + H$	$6.367 \times 10^{11}$	0.00	4305	see text
R48	$C_{12}H_{10} + C_6H_5 \leftrightarrow p\text{-TERPH} + H$	$3.183 \times 10^{11}$	0.00	4305	see text
R49	$o-C_{12}H_9 + C_6H_5 \rightarrow o\text{-TERPH}$	$1.00 \times 10^{13}$	0.00	0	est.
R50	$m-C_{12}H_9 + C_6H_5 \rightarrow m\text{-TERPH}$	$1.00 \times 10^{13}$	0.00	0	est.
R51	$p-C_{12}H_9 + C_6H_5 \rightarrow p\text{-TERPH}$	$1.00 \times 10^{13}$	0.00	0	est.
R52	$o\text{-TERPH} \rightarrow o-C_{12}H_9 + C_6H_5$	$2.92 \times 10^{15}$	0.00	109812	see text
R53	$m\text{-TERPH} \rightarrow m-C_{12}H_9 + C_6H_5$	$2.92 \times 10^{15}$	0.00	109812	see text
R54	$p\text{-TERPH} \rightarrow p-C_{12}H_9 + C_6H_5$	$2.92 \times 10^{15}$	0.00	109812	see text
R55	$o\text{-TERPH} \leftrightarrow \text{TRIPH} + H_2$	$1.50 \times 10^{15}$	0.00	84700	see text
R56	$o-C_{12}H_9 + o-C_6H_4 \leftrightarrow \text{TRIPH} + H$	$1.00 \times 10^{14}$	0.00	38000	see text
R57	$C_{12}H_8 + o-C_6H_4 \leftrightarrow \text{TRIPH}$	$4.96 \times 10^9$	0.827	-1370	see text
Biphenylene and Acenaphthylene					
R58	$o-C_6H_4 + o-C_6H_4 \leftrightarrow C_{12}H_8$	$4.96 \times 10^9$	0.827	-1370	17
R59	$o-C_{12}H_9 \rightarrow \text{BIPHENH}$	$5.00 \times 10^{12}$	0.00	31056	54 <sup>c</sup>
R60	$\text{BIPHENH} \rightarrow o-C_{12}H_9$	$3.00 \times 10^{13}$	0.00	19350	54 <sup>c</sup>
R61	$\text{BIPHENH} \rightarrow C_{12}H_8 + H$	$5.00 \times 10^{13}$	0.00	38223	54 <sup>c</sup>
R62	$C_{12}H_8 + H \rightarrow \text{BIPHENH}$	$4.00 \times 10^{13}$	0.00	5972	54 <sup>c</sup>
R63	$\text{BIPHENH} \rightarrow \text{BENZOH}$	$1.00 \times 10^{13}$	0.00	31056	54 <sup>c</sup>
R64	$\text{BENZOH} \rightarrow \text{BIPHENH}$	$1.00 \times 10^{13}$	0.00	46345	54 <sup>c</sup>
R65	$\text{BENZOH} \rightarrow \text{BENZO}+H$	$5.00 \times 10^{13}$	0.00	41567	54 <sup>c</sup>
R66	$\text{BENZO} + H \rightarrow \text{BENZOH}$	$1.00 \times 10^{14}$	0.00	1911	54 <sup>c</sup>
R67	$\text{BENZOH} \rightarrow \text{A2R5} + H$	$1.00 \times 10^{13}$	0.00	44673	54 <sup>c</sup>



Table 1. continued

	reaction	A	n	E <sub>a</sub>	ref
Biphenylene and Acenaphthylene					
R68	C <sub>12</sub> H <sub>10</sub> → C <sub>6</sub> H <sub>5</sub> CHC <sub>5</sub> H <sub>4</sub>	1.00 × 10 <sup>14</sup>	0.00	109412	54 <sup>c</sup>
R69	C <sub>6</sub> H <sub>5</sub> CHC <sub>5</sub> H <sub>4</sub> → C <sub>12</sub> H <sub>10</sub>	1.00 × 10 <sup>13</sup>	0.00	76445	54 <sup>c</sup>
R70	C <sub>6</sub> H <sub>5</sub> CHC <sub>5</sub> H <sub>4</sub> → BENZO + H <sub>2</sub>	5.00 × 10 <sup>13</sup>	0.00	56617	54 <sup>c</sup>
R71	C <sub>6</sub> H <sub>5</sub> CHC <sub>5</sub> H <sub>4</sub> → A2RS + H <sub>2</sub>	5.00 × 10 <sup>13</sup>	0.00	60917	54 <sup>c</sup>
R72	C <sub>12</sub> H <sub>8</sub> → C <sub>6</sub> H <sub>4</sub> oct	6.152 × 10 <sup>14</sup>	0.00	77387.6	p.w.
R73	C <sub>6</sub> H <sub>4</sub> oct → C <sub>12</sub> H <sub>8</sub>	7.482 × 10 <sup>12</sup>	0.00	4059.6	p.w.
R74	C <sub>6</sub> H <sub>4</sub> oct → BENZOHyI	1.205 × 10 <sup>13</sup>	0.00	13712.9	p.w.
R75	BENZOHyI → C <sub>6</sub> H <sub>4</sub> oct	5.321 × 10 <sup>13</sup>	0.00	31139.8	p.w.
R76	BENZOHyI → BENZO	1.941 × 10 <sup>13</sup>	0.00	10615.0	p.w.
R77	BENZO → BENZOHyI	4.188 × 10 <sup>13</sup>	0.00	75265.9	p.w.
R80	BENZO → A2RS	4.699 × 10 <sup>14</sup>	0.00	77831.2	p.w.
R81	C <sub>10</sub> H <sub>7</sub> -1 + C <sub>2</sub> H <sub>2</sub> ↔ A2RS + H	1.87 × 10 <sup>7</sup>	1.787	3262	21
Phenylacetylene					
R90	C <sub>6</sub> H <sub>5</sub> +C <sub>2</sub> H <sub>2</sub> ↔ C <sub>6</sub> H <sub>5</sub> CHCH	1.345 × 10 <sup>6</sup>	2.05	3720	22 (/2)
R91	C <sub>6</sub> H <sub>5</sub> CHCH ↔ C <sub>8</sub> H <sub>6</sub> + H	3.80 × 10 <sup>11</sup>	0.82	38910	22
R92	C <sub>6</sub> H <sub>5</sub> CHCH ↔ C <sub>6</sub> H <sub>4</sub> CHCH <sub>2</sub>	2.04 × 10 <sup>10</sup>	0.70	27500	22
R94	C <sub>8</sub> H <sub>6</sub> + H ↔ C <sub>6</sub> H <sub>4</sub> C <sub>2</sub> H + H <sub>2</sub>	3.23 × 10 <sup>7</sup>	2.095	15842	53 (×1.5)
R97	o-C <sub>6</sub> H <sub>4</sub> + C <sub>2</sub> H <sub>2</sub> ↔ C <sub>8</sub> H <sub>6</sub>	2.00 × 10 <sup>13</sup>	0.00	20000	74
Diphenylethyne and Phenanthrene					
R98	C <sub>8</sub> H <sub>6</sub> + C <sub>6</sub> H <sub>5</sub> → DPE + H	1.00 × 10 <sup>13</sup>	0.00	7648	see text
R99	DPE+H → C <sub>8</sub> H <sub>6</sub> + C <sub>6</sub> H <sub>5</sub>	4.00 × 10 <sup>14</sup>	0.00	9691	see text
R100	o-C <sub>12</sub> H <sub>9</sub> + C <sub>2</sub> H <sub>2</sub> ↔ PHEN + H	1.87 × 10 <sup>7</sup>	1.787	3262	33
R101	C <sub>8</sub> H <sub>6</sub> + C <sub>6</sub> H <sub>5</sub> ↔ PHEN + H	9.55 × 10 <sup>11</sup>	0.00	4305	33
R112	C <sub>12</sub> H <sub>10</sub> + C <sub>2</sub> H <sub>2</sub> → PHENH	16.92	2.60	42193	86
R113	PHENH → PHEN + H <sub>2</sub>	4.73 × 10 <sup>9</sup>	0.797	17176	86
Naphthalene					
R149	o-C <sub>6</sub> H <sub>4</sub> + C <sub>6</sub> H <sub>6</sub> → BICYCLO	1.1618 × 10 <sup>4</sup>	2.526	5915.9	66, see text
R150	BICYCLO → o-C <sub>6</sub> H <sub>4</sub> + C <sub>6</sub> H <sub>6</sub>	4.910 × 10 <sup>16</sup>	0.00	66811	66, see text
R151	BICYCLO ↔ C <sub>10</sub> H <sub>8</sub> + C <sub>2</sub> H <sub>2</sub>	7.458 × 10 <sup>14</sup>	0.0956	54780.1	66
R152	C <sub>6</sub> H <sub>4</sub> CHCH <sub>2</sub> + C <sub>2</sub> H <sub>2</sub> ↔ C <sub>10</sub> H <sub>8</sub> + H	2.5 × 10 <sup>29</sup>	-4.43	26400	est. <sup>d</sup>
R153	C <sub>6</sub> H <sub>4</sub> C <sub>2</sub> H + C <sub>2</sub> H <sub>2</sub> ↔ C <sub>10</sub> H <sub>7</sub> -1	1.87 × 10 <sup>7</sup>	1.787	3262	est. <sup>c</sup>
R155	C <sub>10</sub> H <sub>7</sub> -1 + H(+M) ↔ C <sub>10</sub> H <sub>8</sub> (+M)	1.00 × 10 <sup>14</sup>	0.00	0	est. <sup>b</sup>
Phenyl Decomposition					
R161	C <sub>6</sub> H <sub>5</sub> (+AR) ↔ o-C <sub>6</sub> H <sub>4</sub> + H(+AR)	4.30 × 10 <sup>12</sup>	0.62	77300	74 <sup>b</sup>
R163	o-C <sub>6</sub> H <sub>4</sub> ↔ C <sub>4</sub> H <sub>2</sub> + C <sub>2</sub> H <sub>2</sub>	1.20 × 10 <sup>18</sup>	-0.34	87776	74
R166	C <sub>6</sub> H <sub>2</sub> + H ↔ C <sub>6</sub> H <sub>3</sub>	1.10 × 10 <sup>30</sup>	-4.92	10800	77
R168	C <sub>4</sub> H <sub>2</sub> + C <sub>2</sub> H ↔ C <sub>6</sub> H <sub>2</sub> + H	3.00 × 10 <sup>13</sup>	0.00	0	74
R171	z-C <sub>6</sub> H <sub>4</sub> + H ↔ C <sub>6</sub> H <sub>3</sub> + H <sub>2</sub>	1.33 × 10 <sup>6</sup>	2.53	9240	32
R195	C <sub>2</sub> H + H <sub>2</sub> ↔ C <sub>2</sub> H <sub>2</sub> + H	4.90 × 10 <sup>5</sup>	2.50	560	32
R197	C <sub>2</sub> H + C <sub>2</sub> H <sub>2</sub> ↔ C <sub>4</sub> H <sub>2</sub> + H	9.60 × 10 <sup>13</sup>	0.00	0	77

<sup>a</sup>Modified within the uncertainty provided in ref 81. <sup>b</sup>Reaction with falloff parameters. <sup>c</sup>E<sub>a</sub> from ref 54; A value estimated. <sup>d</sup>Reaction rate constant for C<sub>6</sub>H<sub>5</sub> + C<sub>2</sub>H<sub>2</sub> ↔ C<sub>8</sub>H<sub>6</sub> + H at 7600 Torr.<sup>20</sup> <sup>e</sup>High-pressure limit for C<sub>10</sub>H<sub>7</sub> + C<sub>2</sub>H<sub>2</sub>.<sup>21</sup>

are reported in the Supporting Information, including for each experiment the actual conditions (pressure, temperature, and reaction time) as well as the mole fractions of the major products.

Before proceeding with the discussion, it is worth mentioning the fact that the reaction rate constants were adjusted mainly on the basis of the experimental sets having accurate carbon recovery (initial concentration of phenyl iodide around 50 ppm or lower). In particular, extensive sensitivity analyses were performed to determine the parameters to be adjusted in order to improve the accuracy of the simulations with respect to the experimental profiles. Due to the complexity of the system in consideration, a complete description of the sensitivity analysis results is not practical. On the other hand, tables containing the sensitivity coefficients for the most relevant reactions have been provided in the Supporting Information for each major stable product and for selected experimental conditions.

Once the model was validated, rates of production analyses were utilized to obtain additional information on the pathways relevant for the formation and the consumption of the major products. These analyses provide the rates at which the species are produced or consumed by a specific reaction during the whole progress of the combustion process. Thus, they provide evidence of the importance of specific pathways for the formation/consumption of the species in consideration. Of course, the rate of production analyses can be utilized with confidence only for those conditions where the agreement between experiments and simulations is sufficiently accurate. Since a complete description of the rate of production analyses is not practical, only a few results are reported throughout the article when relevant to the discussion (Figures 8, 24, 27, and 29).

**3.1. Phenyl Pyrolysis.** A typical chromatogram obtained from the pyrolysis of phenyl iodide at a nominal pressure of 50

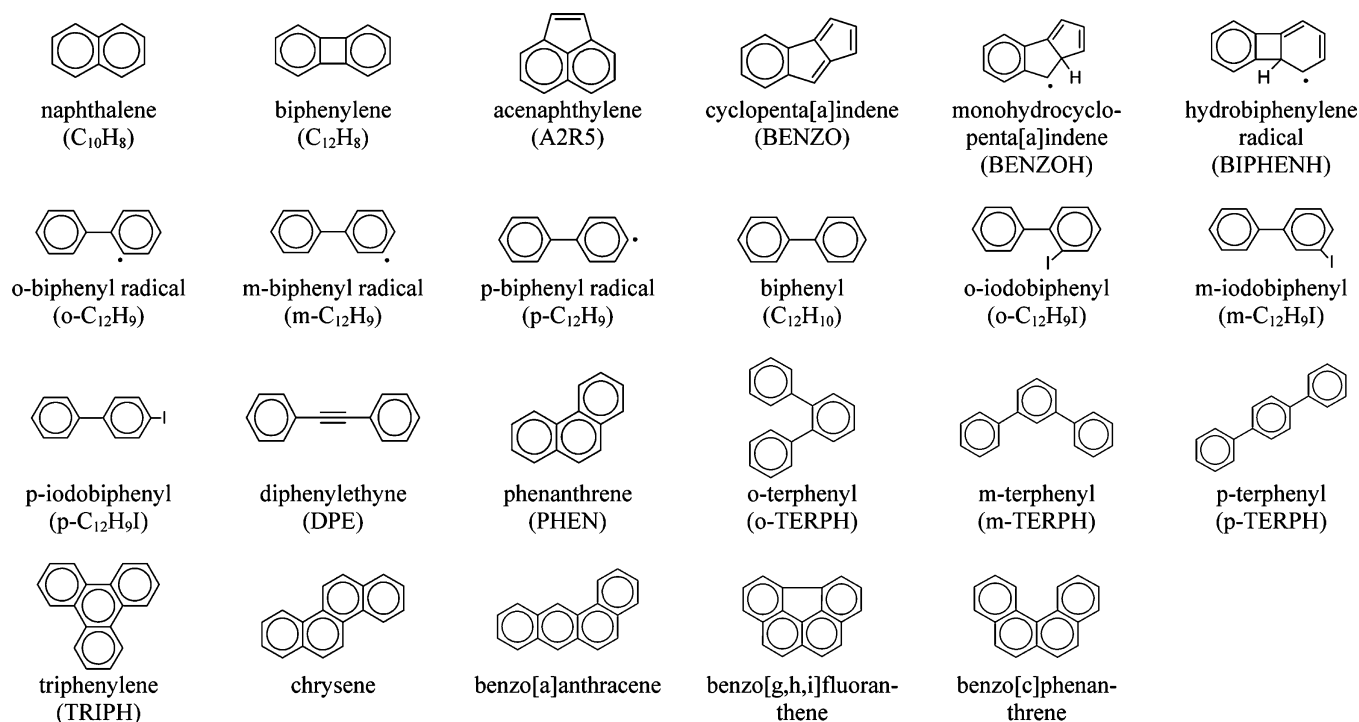


Figure 2. Molecular structures of the major polycyclic aromatic hydrocarbons discussed in the text.

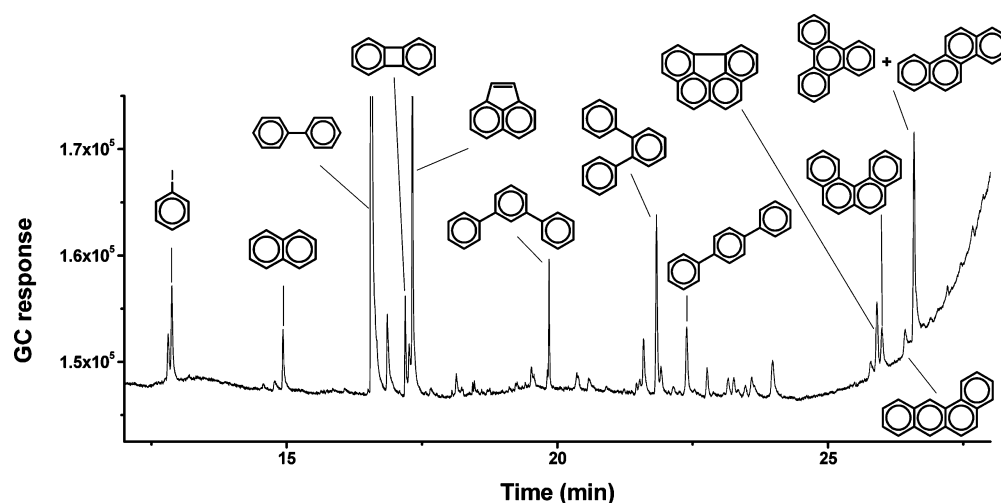


Figure 3. Typical chromatographic signal for phenyl radical pyrolysis. FID detector, DB-17ms column.

atm and initial mole fraction of 50.6 ppm is reported in Figure 3. The chromatogram clearly shows the complexity of the reaction system in consideration. Although only the major products are annotated, several additional peaks were detected. Such peaks correspond to compounds produced in trace amounts during the reaction, including among the others indene, di-iodobenzenes, fluorene, 1-iodonaphthalene, anthracene, phenanthrene, iodobiphenyls, 2-phenylindene, 1-phenyl-naphthalene, 2-phenylnaphthalene, pyrene, and other unidentified C18 species. Although the formation of such compounds suggests the presence of several minor mechanistic pathways, from a practical point of view only the major products and the associated reactions were considered for the development of the chemical kinetic model. The main results are reported below. For brevity purposes, only the graphs containing the results obtained at nominal pressure of 25 atm and initial mole

fraction of 54.2 ppm are shown in the article. The remaining graphs have been included in the Supporting Information.

**3.1.1. Phenyl Iodide Decomposition.** A comprehensive analysis of the C–I fission in phenyl iodide decomposition has been performed by Tranter et al.<sup>17</sup> in their recent investigation of the self-reaction between phenyl radicals. The authors compared the experimental data present in literature<sup>41–44</sup> with their experimental results as well as the reaction rate constants obtained with a Gorin model RRKM calculation. It is not the purpose of the present work to repeat a detailed analysis of the thermal decomposition of phenyl iodide. Thus, only a brief discussion of the main results obtained using the HPST is presented below.

The normalized profiles for the decomposition of phenyl iodide are reported in Figure 4a. The experiments do not indicate any significant dependence on the initial mole fraction

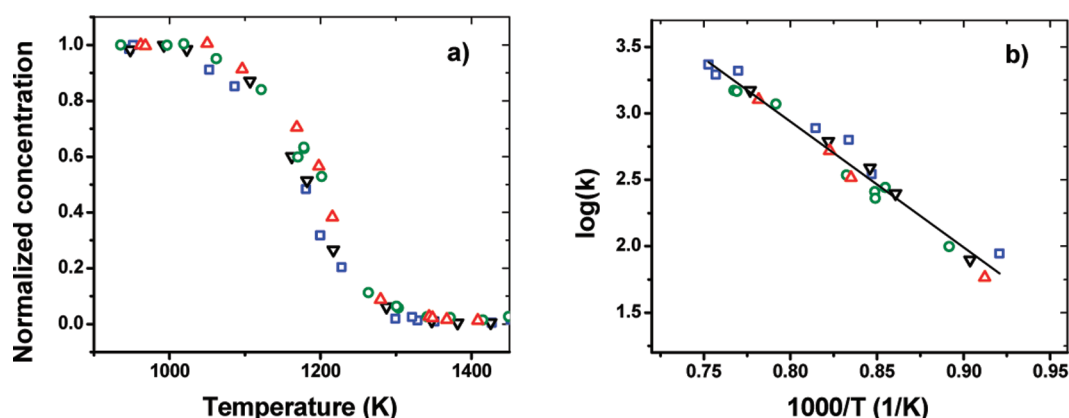


**Figure 4.** (a) Normalized phenyl iodide decomposition and (b) Arrhenius plot of the measured apparent reaction rate constant for phenyl iodide decomposition between 1086 and 1328 K,  $k$  in  $\text{s}^{-1}$ . Green circles,  $[\text{C}_6\text{H}_5\text{I}]_0 = 50.6$  ppm,  $p \approx 50$  atm; red triangles,  $[\text{C}_6\text{H}_5\text{I}]_0 = 95.6$  ppm,  $p \approx 50$  atm; blue squares,  $[\text{C}_6\text{H}_5\text{I}]_0 = 26.6$  ppm,  $p \approx 50$  atm; black down-triangles,  $[\text{C}_6\text{H}_5\text{I}]_0 = 54.2$  ppm,  $p \approx 25$  atm; solid line, linear interpolation.

of the reactant or on the reaction pressure. At the conditions of the present study the experimental decay of phenyl iodide is not only due to the C–I bond fission leading to the formation of phenyl radicals and iodine atoms, but it is also influenced by the secondary reactions of the phenyl iodide with different product species including phenyl radicals and hydrogen atoms when present in the system. Moreover, the recombination reaction between phenyl radicals and iodine atoms to form  $\text{C}_6\text{H}_5\text{I}$  will play a relevant role lowering the apparent decomposition rate. Thus, the high-pressure conditions implemented in the present investigation do not allow the determination of the absolute rate constant for the phenyl iodide decomposition, although an apparent overall reaction rate constant can be derived from the Arrhenius plot presented in Figure 4b. The Arrhenius expression of the apparent reaction rate constant is  $k \approx 3.24 \times 10^{10} \exp(-21797/T)$  ( $\text{s}^{-1}$ ).

The high-pressure-limit reaction rate constant for the C–I fission derived by Kumaran et al.<sup>42</sup> on the basis of their low-pressure experiments best fits our experimental data, although the phenyl iodide concentrations are slightly overpredicted by the model when the reverse reaction rate constant is calculated using the equilibrium constant. Better agreement between experiments and simulations was obtained assuming a temperature-independent reaction rate constant  $k_2$  for the recombination between phenyl radicals and iodine atoms (Table 1). In addition, as suggested by Tranter et al.,<sup>17</sup> the branching ratios for the two main unimolecular decomposition channels forming  $\text{C}_6\text{H}_5 + \text{I}$  and  $o\text{-C}_6\text{H}_4 + \text{HI}$  were assumed to be  $\sim 94\%$  and  $6\%$ , respectively. The rate parameters for the two unimolecular decomposition reactions are reported in Table 1 (R1, R2, and R3). Figure 5 shows the excellent agreement between the phenyl iodide experimental profiles and the modeling results for the experiments conducted at nominal pressure of 25 atm and initial phenyl iodide mole fractions of around 50 ppm. Similar agreement was obtained for the data set at 50 atm (Figure 3S, Supporting Information).

**3.1.2. Formation of Benzene, Biphenyl, and Substituted Biphenyls.** As already mentioned in the Introduction, biphenyl is one of the most important building blocks for the formation of large PAH compounds, and it constitutes the primary product of the radical–radical recombination between phenyl radicals.<sup>15,16</sup> If the only reaction channel available for the self-reaction between phenyl radicals was the radical–radical recombination, biphenyl would be the major product of the

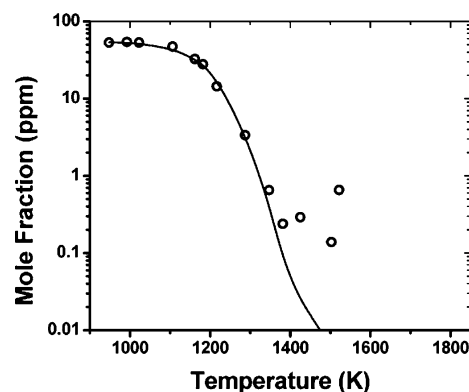


**Figure 5.** Phenyl iodide decomposition. Circles, experiments; line, simulation.  $[\text{C}_6\text{H}_5\text{I}]_0 = 54.2$  ppm,  $p \approx 25$  atm.

phenyl iodide decomposition. Only small amounts of other stable compounds would be measured, including for example benzene from the recombination of the phenyl radicals with hydrogen atoms. Surprisingly, the experiments indicated that a large amount of benzene is produced even at low temperatures where the hydrogen atoms are present in the system only in small concentrations. As shown in Figure 6a, at temperatures between 1250 and 1400 K, around 25% of the phenyl radicals produced from the phenyl iodide decomposition is converted into benzene. The results presented in Figure 6a also indicate that the chemical mechanisms which lead to the formation/consumption of benzene are not dependent on either the initial phenyl iodide mole fraction or reaction pressure. Moreover, the peculiar shape of the profiles, characterized by a rapid increase up to 1250 K in correspondence with the end of the phenyl iodide decay followed by a slight decrease up to 1450 K and a more rapid decrease at higher temperatures, suggests that at least two reaction mechanisms are responsible for the formation of benzene. The main mechanism was proposed and studied in detail by Tranter et al.,<sup>17</sup> who highlighted for the first time the complexity of the self-reaction between phenyl radicals. The authors examined the different reaction channels by high-level computational methods and concluded that the reaction between phenyl radicals does not proceed only through recombination to form biphenyl, but also through H-abstraction to form benzene and *ortho*-, *meta*-, and *para*-benzynes. The key role of the benzyne, in particular of *o*-benzyne, will be discussed later in the text in relation to the

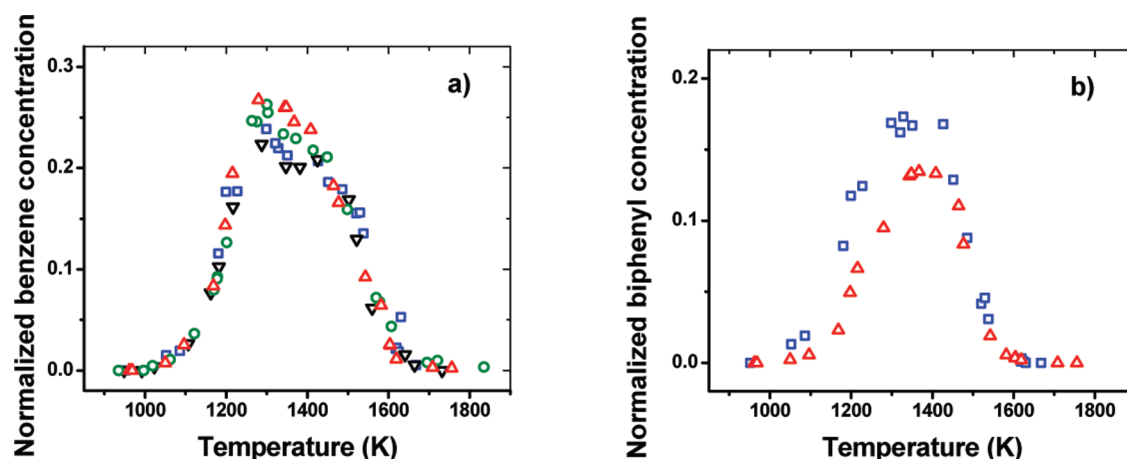


**Figure 6.** (a) Normalized benzene decomposition and (b) normalized biphenyl decomposition. Green circles,  $[C_6H_5I]_0 = 50.6$  ppm,  $p \approx 50$  atm; red triangles,  $[C_6H_5I]_0 = 95.6$  ppm,  $p \approx 50$  atm; blue squares,  $[C_6H_5I]_0 = 26.6$  ppm,  $p \approx 50$  atm; black down-triangles,  $[C_6H_5I]_0 = 54.2$  ppm,  $p \approx 25$  atm.

formation of terphenyls, biphenylene, acenaphthylene, naphthalene, and the four-ring compounds.

The reaction rate constants associated with the two competing channels for the self-reaction between phenyl radicals, i.e., the recombination channel and the H-abstraction channel, were calculated by Tranter et al.<sup>17</sup> using high-level theoretical calculations and transition state theory. As suggested by the authors, the branching ratio for the three H-abstraction channels leading to *o*-benzynes + benzene, *m*-benzynes + benzene, and *p*-benzynes + benzene was estimated as 0.40:0.40:0.20, and the corresponding reaction rate constants taken as the high-pressure-limit expressions calculated in ref 17 reduced, within the stated error limits, by a factor of 2 (reactions R21–R23, Table 1). A similar reduction, within the error limits, in the corresponding low-pressure expressions was applied by Tranter et al. in order to improve the agreement between the simulations and the low-pressure experiments, suggesting that the rate constant may be off by a factor of 2 across the entire pressure range. The isomerization between the three benzyne isomers has been studied theoretically by Moskaleva et al.,<sup>45</sup> who derived reaction rate constant expressions utilized in the present work (R24 and R25). The *p*-benzyne can also easily undergo a Bergman decyclization to form 1,5-hexadiyn-3-ene. The corresponding reaction rate constant was estimated on the basis of a reaction barrier of 17.8 kcal/mol as calculated in ref 45 (R26). Finally the reaction rate constant for the recombination reaction was reduced by a factor of 2 compared to the expression derived by Tranter et al.<sup>17</sup> for a pressure of 100 atm (R20). This modification, within the estimated uncertainty provided by the authors, lead to the improvement of the modeling results not only for biphenyl but also for other intermediates such as benzene and *o*-terphenyl. In fact, many of the simulation profiles showed a strong sensitivity toward the parameters of reaction R20 as indicated in the sensitivity analysis tables in the Supporting Information. This observation clearly implies that the modeling results are sensitive to the branching ratio between the recombination and the abstraction channels of the phenyl + phenyl reaction.

We mentioned earlier the fact that the benzene profiles in Figure 6a suggest the relevance of a second reaction mechanism which lead to the formation of benzene. Such a mechanism involves the reaction between phenyl radical and hydrogen iodide to form benzene and iodine atoms. Hydrogen iodide derives mainly from the direct decomposition of  $C_6H_5I$  into *o*-

$C_6H_4 + HI$  as described in section 3.1.1 and at later times in the reaction by the abstraction reaction between phenyl iodide and hydrogen atoms (R4 in Table 1). Thus, although the phenyl iodide is usually considered as a clean source of phenyl radicals, its chemical properties lead to the formation of halogenated species, in this case HI, which can subsequently influence the formation of the intermediates of interest, in this case benzene, derived from the reaction of the phenyl radicals.

An estimated temperature-independent rate constant for the reaction between  $C_6H_5$  and HI has been used in the present model (reaction R5, Table 1). In view of the decreased reactivity of the phenyl radical compared to the hydrogen atom,  $k_5$  is an order of magnitude lower than the reaction rate constant for reaction R19,  $H + HI \rightarrow H_2 + I$  (ref 46), although nearly twice the value extrapolated from the expression derived by Rodgers et al.,<sup>47</sup> who experimentally investigated the reaction at relatively low temperatures (648–773 K).

The model simulates with good accuracy the profiles of biphenyl for the experiments conducted at 25 atm with initial  $C_6H_5I$  mole fraction of 54.2 ppm (Figure 7) and at 50 atm with 26.6 ppm of reactant (Figure 36a, Supporting Information). Above 1450 K the biphenyl concentrations are overpredicted by the model, but as discussed later in the text this discrepancy is mainly due to the fact that the model is not able to correctly predict the chemistry relevant to high-temperature conditions. The remaining  $C_{12}H_{10}$  profiles (Figure 36b,c, Supporting

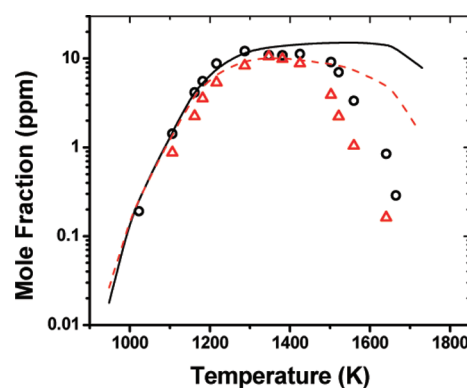


**Figure 7.** Black circles, benzene experiments; black line, benzene simulation; red triangles, biphenyl experiments; and red dashed line, biphenyl simulations.  $[C_6H_5I]_0 = 54.2$  ppm,  $p \approx 25$  atm.



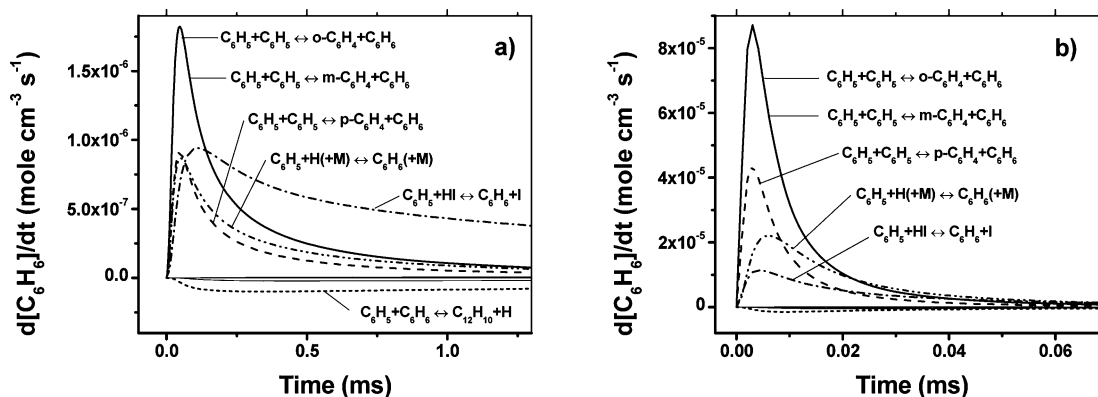


Figure 8. Analysis of the rate of benzene production,  $[C_6H_5I]_0 = 54.2$  ppm: (a)  $T = 1217$  K,  $p = 29.1$  atm and (b)  $T = 1502$  K,  $p = 25.3$  atm.

Information) are overestimated by the model even at low temperatures, in particular in the case of initial mole fraction of 95.6 ppm. The drop in the relative carbon balance described above in relation to Figure 1a suggests the presence of pathways for the formation of larger compounds which are not measured in the present study. Such pathways could be responsible for the consumption of biphenyl at relatively high phenyl radical concentrations. This hypothesis is supported by the comparison between the normalized experimental profiles for biphenyl in the case of initial phenyl iodide mole fraction of 26.6 and 95.6 ppm at a nominal pressure of 50 atm (Figure 6b). In contrast with the case of benzene where no dependence on the pressure and the initial  $C_6H_5I$  mole fraction was observed (Figure 6a), the normalized profiles show a significant drop in the biphenyl concentrations at higher phenyl iodide mole fractions.

Different considerations apply for the simulation of the benzene profiles. As shown in Figure 7 the initial slope of formation is well reproduced by the model. This is valid for most of the experimental sets with the exception of the set conducted with initial phenyl iodide mole fraction of 95.6 ppm for which the initial slope is underpredicted (Figure 36c). The rate of production analysis performed at 1217 K and 29.1 atm with initial mole fraction of 54.2 ppm shows that at the beginning the formation of benzene is mainly influenced by the abstraction channel between phenyl radicals with smaller contributions from the reaction between phenyl and hydrogen iodide and from the recombination between phenyl and hydrogen<sup>48</sup> (Figure 8a). In Figure 8a the lines for the *o*- and *m*-benzynes channels are superimposed. As the reaction progresses, the reaction  $C_6H_5 + HI$  becomes the predominant pathway for the formation of benzene. Its contribution is essential for the accurate description of the benzene profiles in the low-temperature range of the present study as shown in Figure 9, where the modeling results from the complete model are compared to the results obtained when the reaction  $C_6H_5 + HI \leftrightarrow C_6H_6 + I$  is removed (experimental set with initial concentration of 54.2 ppm and nominal pressure of 25 atm). Similar reactions between  $C_6H_5$  and  $HX$  could also be relevant when a generic  $C_6H_5X$  precursor is utilized, i.e.,  $C_6H_5Cl$  or  $C_6H_5Br$ . In these cases the reaction rate constants are expected to be lower than  $k_5$  since in general the  $H-X$  bond would be stronger than the  $H-I$  bond.

While the benzene profiles are well reproduced for temperatures below 1350 K, at higher temperatures the model fails to simulate accurately the decay observed in the experimental data. In particular, above 1450 K where the

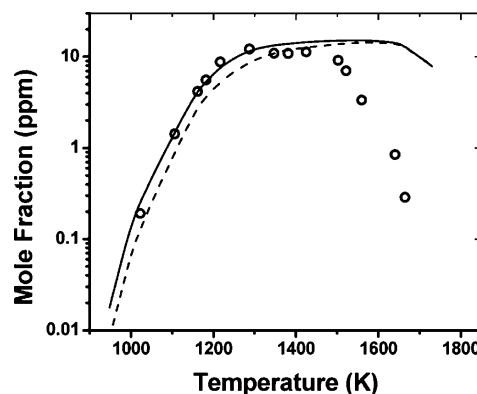


Figure 9. Benzene,  $[C_6H_5I]_0 = 54.2$  ppm,  $p \approx 25$  atm. Black circles, experiments; solid line, model in Table 1; dashed line, model in Table 1 omitting  $C_6H_5 + HI \leftrightarrow C_6H_6 + I$ .

experimental concentrations drop rapidly, the model predicts an increase in the benzene mole fraction up to around 1600 K (Figure 7). The rate of production analysis performed at 1502 K (Figure 8b) indicates that at high temperatures the formation of benzene is still mainly due to the H-abstraction channel. In comparison to the low-temperature case, the contributions provided by the reaction R5 and R44 are only minor. In order to understand if other reaction rate parameters could be responsible for the overestimation observed at high temperatures, the sensitivity analysis was also performed at the same conditions which confirmed the importance of the above-mentioned reactions (Figure 10). The sensitivity analysis also indicates a strong dependence on the rate parameters of

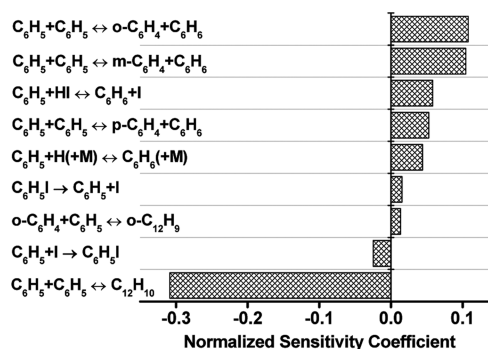
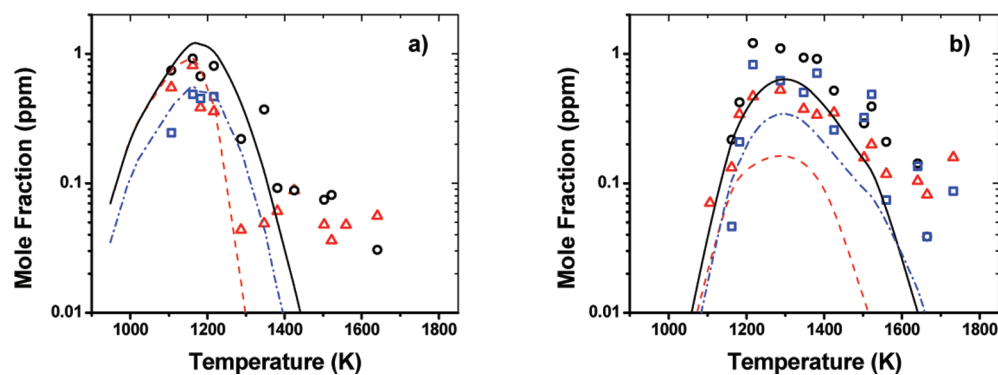


Figure 10. Sensitivity analysis for benzene.  $[C_6H_5I]_0 = 54.2$  ppm,  $T = 1502$  K,  $p = 25.3$  atm,  $t = 1.68$  ms.



**Figure 11.** (a) Red triangles, *o*-iodobiphenyl experiments; red dashed line, *o*-iodobiphenyl simulation; black circles, *m*-iodobiphenyl experiments; black line, *m*-iodobiphenyl simulation; blue squares, *p*-iodobiphenyl experiments; blue dash-dotted line, *p*-iodobiphenyl simulation. (b) Red triangles, *o*-terphenyl experiments; red dashed line, *o*-terphenyl simulation; black circles, *m*-terphenyl experiments; black line, *m*-terphenyl simulation; blue squares, *p*-terphenyl experiments; blue dash-dotted line, *p*-terphenyl simulation.  $[C_6H_5I]_0 = 54.2$  ppm,  $p \approx 25$  atm.

reaction R20, the recombination between phenyl radicals to form biphenyl. The modification of the related reaction rate parameters within the corresponding uncertainties does not lead to a substantial improvement of the benzene profile at high temperatures without affecting the accuracy of the predictions for other compounds, i.e., biphenyl and benzene, at low temperatures. This is clearly an indication that the model is not complete and requires the addition of reaction pathways which reduce the predicted formation of benzene at high temperatures. We will analyze this issue in more detail later in the article in correspondence with the discussion about the formation of the light hydrocarbons (section 3.1.7).

In addition to benzene and biphenyl, iodobiphenyls have been measured in the low-temperature range of our experiments. Once again, the measurement of halogenated species indicates that the phenyl iodide is not an ideal source of phenyl radicals. Although the study of the iodobiphenyls' chemistry is not the focus of the present work, it is essential to include the corresponding reactions in the chemical kinetic model in order to obtain a better agreement between simulations and experimental results for the low-temperature profiles of several species, including benzene, biphenyl, and the terphenyls. The experimental measurement of the three iodobiphenyl isomers is also important to define the primary products of the addition between the phenyl radical produced by decomposition of the phenyl iodide precursor and the precursor itself. Such addition process becomes relevant at the high pressures implemented in the present study or at low pressures when large concentrations of the precursor are utilized. A brief analysis of the main experimental and modeling results regarding the iodobiphenyls is provided below which can serve as reference for future investigations on the decomposition of phenyl radical precursors and the related chemistry.

As soon as the phenyl iodide starts decomposing, iodobiphenyls are produced indicating a strong correlation between the two processes. In fact, the three isomeric forms are mainly generated from the reaction between  $C_6H_5I$  and  $C_6H_5$  in a similar fashion as the reaction between phenyl radical and benzene leads to the formation of biphenyl and hydrogen.<sup>49</sup> The pre-exponential factors of the corresponding reaction rate constants have been adjusted based on the multiplicity of the specific reaction pathway (R7–R9, Table 1). Once produced, the iodobiphenyls can dissociate to form biphenyl radicals and iodine atoms (R10–R15). The dissociation and recombination

reaction rate constants have been assumed similar to the ones relative to the phenyl iodide decomposition, i.e., R1 and R2.

The experimental profiles are well reproduced by the model as shown in Figures 11a and 37 (Supporting Information). In particular, for the sets in Figures 11a and 37a, both the shapes of the profiles and the maximum mole fractions are accurately predicted. The *m*-iodobiphenyl is the isomer present in larger amounts in these experiments, while the *p*-iodobiphenyl shows the lowest concentrations. It is important to notice how the model correctly replicates such hierarchy. When we analyze the experimental results obtained with higher concentrations of phenyl iodide (Figure 37b,c), we notice that the *o*-iodobiphenyl is the most abundant among the three isomers. This indicates the presence of alternative pathways for the formation or consumption of the iodobiphenyls compared to the case shown in Figure 11a. Although the shapes of the profiles are well reproduced by the model, the calculated mole fractions are overestimated compared to the experiments, especially when 95.6 ppm of phenyl iodide are pyrolyzed (Figure 37c); thus, we can hypothesize that additional consumption reactions should be added to the model. Such reactions include for example the reactions between the iodobiphenyls and  $C_6H_5$  or H.

**3.1.3. Terphenyls.** The obvious step in the growth toward larger PAH compounds which follows the formation of biphenyl is the subsequent addition of a phenyl radical to form the terphenyls. The mechanism of phenylation of biphenyl to form *o*-, *m*-, and *p*-terphenyls was proposed by Brooks et al.,<sup>50</sup> who measured trace amounts of these polyphenyls in their study on benzene pyrolysis at relatively low temperatures (873–1036 K). The *o*-, *m*-, and *p*-terphenyls are well separated by the GC method implemented in the present study as shown in Figure 3 and mole fraction profiles could be obtained for all three isomers (Figure 11b). The experimental profiles reach a maximum around 1275–1300 K with the *m*-terphenyl being the most abundant among the isomers. The mole fraction of *o*-terphenyl is lower not only compared to the mole fraction of *m*-terphenyl but also compared to the mole fraction of *p*-terphenyl. This experimental finding is surprising since from a simple analysis of the multiplicity of the specific reaction pathways for the addition between biphenyl and phenyl we would expect similar yields of the *o*- and *m*-terphenyls, in proportion twice the yield of *p*-terphenyl. From a chemical kinetic point of view, the experimental results suggest that *o*-terphenyl is consumed by reactions which does not involve the other isomers or that

additional reaction pathways are involved in the formation of the three terphenyls. Both hypotheses are in principle correct, although only one has a substantial impact in the modeling results as discussed below.

*o*-Terphenyl can undergo a cyclodehydrogenization process to form triphenylene (R55 in Table 1). The corresponding reaction rate constant has been estimated on the basis of the rate constant proposed by Zhang et al.<sup>51</sup> for the cyclodehydrogenization of *cis*-1,2-diphenylethene to form phenanthrene. Due to the high activation energy involved in the process (84.7 kcal/mol), its contribution is not sufficient to justify the significant difference between the experimental *o*- and *m*-terphenyls' mole fractions especially in consideration of the temperature range of the present study.

We will now consider alternative pathways for the formation of the terphenyls which could explain the discrepancy between the expected concentrations and the experimentally observed ones. As discussed in the previous section, the decomposition of the iodobiphenyls leads to the formation of biphenyl radicals and iodine atoms. Even more significant for the formation of the *o*- and *m*-biphenyl radicals are the reactions of phenyl radical with *o*- and *m*-benzynes, respectively (R27 and R28). The corresponding reaction for the formation of the *p*-C<sub>12</sub>H<sub>9</sub> radical (R29) does not play an important role in the modeling results since the *p*-benzynes radical quickly isomerizes to form 1,5-hexadiyn-3-ene (R26) and is not available for reaction with phenyl. Once produced, the three biphenyl radicals can recombine with an additional phenyl radical to form directly the terphenyls (R49–R51).

We discussed in generic terms about additional pathways to the terphenyls, but we did not explain how these pathways could address our initial question about the unexpected relatively low *o*-terphenyl concentrations. The explanation is found in the fact that the pathway for the formation of *o*-terphenyl from *o*-C<sub>12</sub>H<sub>9</sub> (Figure 2) + C<sub>6</sub>H<sub>5</sub> is not as effective as the corresponding ones for *m*- and *p*-terphenyls even though *o*-C<sub>6</sub>H<sub>4</sub> is the most abundant among the benzyne isomers, which implies a relatively high concentration of *o*-biphenyl radicals compared to the meta and para ones. In fact, the *o*-biphenyl radical can isomerize and form the hydrobiphenylene radical (R59, see Figure 2 for chemical structure) reducing the concentration of *o*-C<sub>12</sub>H<sub>9</sub> available for recombination with phenyl. We will discuss this reaction in the section relative to acenaphthylene formation (section 3.1.4). On the other hand, the *m*-C<sub>12</sub>H<sub>9</sub> and the *p*-C<sub>12</sub>H<sub>9</sub> are mainly consumed by reaction with C<sub>6</sub>H<sub>5</sub> to form *m*- and *p*-terphenyls. In addition, we need to consider that *o*-benzynes not only reacts with phenyl to form the *o*-biphenyl radical but is also consumed by other reactions involved in the formation of different PAH compounds, i.e., biphenylene, naphthalene, and the four-ring species. Such reactions will be discussed later in the article in the corresponding sections.

An additional aspect which affects the formation of *o*-terphenyls is the thermodynamic stability of the compound. Due to the repulsion of the H atoms across the bay, defined as the area delimited by the three aromatic rings, *o*-terphenyl is less stable compared to the *m*- and the *p*-terphenyl isomers by 3–4 kcal/mol based on the calculations performed using the uB3LYP/6-311+G(d,p) method and the ring-conserved isodesmic reaction scheme.<sup>35</sup> The lower stability of the *o*-terphenyl will favor pathways for its consumption compared to the more stable isomers.

The formation of the terphenyls has been included in previous chemical kinetic models.<sup>5</sup> For the purpose of the present investigation, the reaction rate parameters of the reactions involved in the mechanisms of formation of the terphenyls have been estimated as reported in Table 1. In particular, the activation energy for the recombination reactions between the benzyne and the phenyl radical (R27–R29) has been estimated as similar to the barrier calculated by Tokmakov and Lin<sup>22</sup> for the reaction between phenyl radical and acetylene forming the 2-phenylvinyl radical. The approximated reaction rate parameters for the dissociation reactions R30 and R31 respectively for *m*-C<sub>12</sub>H<sub>9</sub> and *p*-C<sub>12</sub>H<sub>9</sub> are analogous to the parameters for the reverse of reaction R27 for which the thermochemical parameters are well established. Likewise, the reactions for the decomposition of the terphenyls into biphenyl radicals + phenyl radicals (R52–R54) are analogous to the reverse of C<sub>6</sub>H<sub>5</sub> + C<sub>6</sub>H<sub>5</sub> ↔ C<sub>12</sub>H<sub>10</sub>. Finally, the reaction rate constants for C<sub>6</sub>H<sub>5</sub> + C<sub>12</sub>H<sub>10</sub> forming terphenyls and H atoms (R46–R48) have been estimated on the basis of the reaction rate constant for C<sub>6</sub>H<sub>5</sub> + C<sub>6</sub>H<sub>6</sub> forming biphenyl + H.<sup>49</sup> The corresponding pre-exponential factors were adjusted based on the multiplicity of the specific pathway.

As shown in Figures 11b and 38 (Supporting Information), the simulation results reproduce the shape of the terphenyl profiles with very good accuracy in particular in relation to the estimated temperature range where the profiles reach the maximum value. It is also noticeable how the relative concentrations between the three isomers are in good agreement with the experiments, with *m*-terphenyl produced in larger amounts compared to *p*-terphenyl and *o*-terphenyl.

The results presented in the current section indicate that in order to have an accurate representation of the phenyl radical chemistry it is necessary to consider the detailed pathways involved in the formation of the terphenyls. A particularly important role is played by the presence of the *o*- and *m*-benzenes as primary reactants involved in the formation of the biphenyl radicals which serve as building blocks for the terphenyls. We will discuss in the next sections how the benzyne chemistry influences the formation of other PAH compounds relevant for the formation of soot.

**3.1.4. Biphenylene and Acenaphthylene.** In view of the formation of substantial amounts of *o*-benzynes radicals by the decomposition of the phenyl iodide (R3), by the H-abstraction between phenyl radicals (R21), and by the isomerization of *m*-benzynes (R24), we would expect biphenylene to be among the major stable products of the decomposition of phenyl iodide. Once again the experimental results do not reflect the expectations. As shown in Figure 12, less than 1 ppm of biphenylene is produced even with initial phenyl iodide mole fraction equal to 95.6 ppm. The production of small amounts of biphenylene is a confirmation of the fact that *o*-benzenes are consumed by other reactions, i.e., the reaction with phenyl radical to form *o*-C<sub>12</sub>H<sub>9</sub> described in the previous section. Figure 12 also indicates that the production of biphenylene is proportional to the initial concentration of the fuel, in agreement with the fact that biphenylene derives from the recombination between *o*-benzynes radicals whose formation is directly linked to the fuel or its primary products as described above. The high-pressure limit reaction rate constant for the recombination between the benzyne radicals has been recently calculated by Tranter et al.<sup>17</sup> and utilized in the present model without any adjustment (R58).

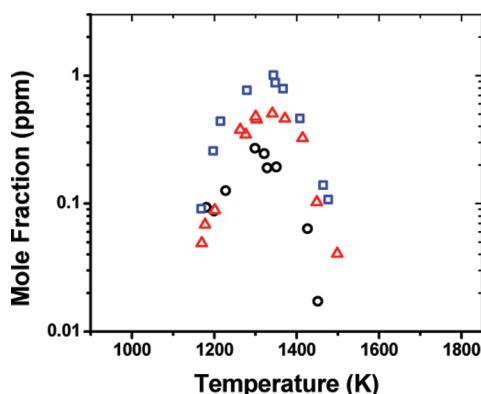


**Figure 12.** Biphenylene experimental concentrations at  $p \approx 50$  atm: black circles,  $[C_6H_5I]_0 = 26.6$  ppm; red triangles,  $[C_6H_5I]_0 = 50.6$  ppm; blue squares,  $[C_6H_5I]_0 = 95.6$  ppm.

While the formation of biphenylene is at least from a descriptive point of view simple, the mechanisms involved in the formation of acenaphthylene are more complex and still not well clarified. Our discussion starts with the simple experimental observation of the fact that acenaphthylene is produced in considerable amounts during the pyrolysis of the phenyl radical. The experimental profiles are reported in Figures 13 and 39 (Supporting Information) and indicate as

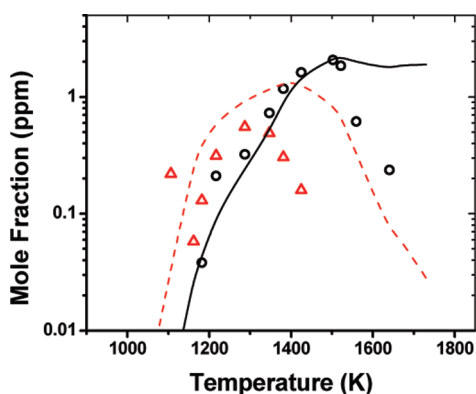


**Figure 13.** Red triangles, biphenylene experiments; red dashed line, biphenylene simulation; black circles, acenaphthylene experiments; black line, acenaphthylene simulation.  $[C_6H_5I]_0 = 54.2$  ppm,  $p \approx 25$  atm.

expected that acenaphthylene is not a primary product of the recombination between phenyl radicals. In fact, its formation does not occur in the low-temperature range of our experiments. As shown in Figures 13 and 39, acenaphthylene profiles are characterized by a rapid increase starting at around 1250 K, which is typical of an isomerization process with relatively high pre-exponential and activation energy or of a process involving secondary products. The profiles reach the maximum at around 1500 K before dropping rapidly at higher temperatures.

The conventional formation pathway for acenaphthylene involves the well-studied reaction between naphthyl radical and acetylene.<sup>21,52</sup> Naphthyl radicals are generally formed through the HACA mechanism<sup>1,2</sup> starting from phenyl and acetylene through the phenylacetylene intermediate. Thus, the whole process requires the addition of three acetylene molecules to a phenyl radical with an intermediate H-abstraction from the

phenylacetylene. The present experiments are performed without acetylene in the initial mixture, and although acetylene is produced at high temperatures, we can exclude the naphthyl + acetylene reaction as relevant to the formation of acenaphthylene. A good proof for this hypothesis is provided by the measurement of the intermediate phenylacetylene. As shown in Figure 14, phenylacetylene is produced in trace

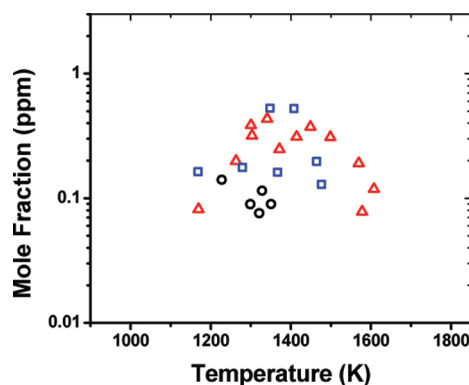


**Figure 14.** Phenylacetylene experimental concentrations at  $p \approx 50$  atm: black circles,  $[C_6H_5I]_0 = 26.6$  ppm; red triangles,  $[C_6H_5I]_0 = 50.6$  ppm; blue squares,  $[C_6H_5I]_0 = 95.6$  ppm.

amounts even when large concentrations of phenyl iodide are pyrolyzed. In addition as discussed in the second part of the paper the presence of much larger concentrations of acetylene would not be sufficient to justify the high mole fractions of acenaphthylene.

Richter et al.<sup>53</sup> reported the presence of large amounts of acenaphthylene in their benzene flame experiments. The authors hypothesized that acenaphthylene is produced through the formation of the hydrobiphenylene radical (see Figure 2 for chemical structure) from the addition between biphenylene and hydrogen, followed by isomerization to acenaphthylene. The proposed pathway is part of a more complex potential energy surface which has been recently studied in details by Shukla et al.<sup>54</sup> using ab initio calculations. The authors explored the possible pathways involved in the isomerization of biphenyl and *o*-biphenyl radical in relation to the formation of several stable compounds, including among the others acenaphthylene.

The theoretical results presented in ref 54 have been included in the model (R59–R71). Due to the complexity of the problem several assumptions were made. First of all only the more stable compounds were considered as possible final products of the isomerization processes. These compounds include biphenylene, acenaphthylene, and cyclopenta[*a*]indene (benzopentalene, BENZO in Figure 2 and Table 1). The activation energies of the elementary reactions are assumed as equal to the relative theoretical barriers. The corresponding pre-exponential factors are estimated on the basis of the values for similar reactions. When a global step is considered, a similar approach was used considering the barrier between the reactants and the maximum energy of the specific path as the activation energy. The pre-exponential was estimated on the basis of the reaction constituting the limiting step in the global process.

The reaction pathway which involves the isomerization of biphenyl (R68–R71) does not play a significant role at the temperature conditions implemented in the present study, although biphenyl is formed in large amounts. In fact, the



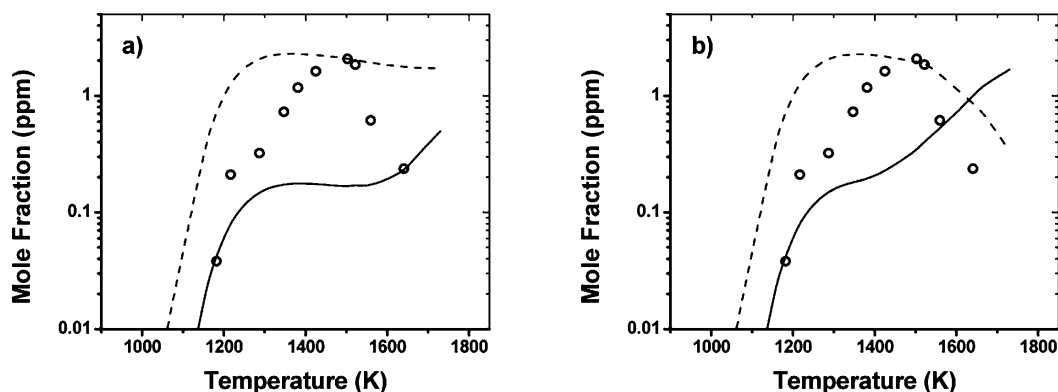


**Figure 15.** Circles, acenaphthylene experiments; solid line, acenaphthylene simulation; dashed line, cyclopenta[*a*]indene simulation. (a) Model in Table 1 omitting reaction R80 and (b) model in Table 1 with  $k_{80}$  calculated from ref 58.  $[C_6H_5I]_0 = 54.2$  ppm,  $p \approx 25$  atm.

entrance barrier of almost 110 kcal/mol is too high to allow a significant flux to enter the potential energy surface. Even a 10-fold increase in the estimated pre-exponential factor does not lead to a significant change in the modeling results. On the other hand, the energy required for the isomerization of the *o*-biphenyl radical is much lower as the corresponding barrier is equal to around 31 kcal/mol (R59). Considering the fact that *o*-biphenyl radicals are formed in considerable amounts by the recombination between phenyl and *o*-benzyne radicals (R27) as discussed in the previous section, we expect the corresponding isomerization (R59) to occur even in the temperature range of our experiments. Thus, we have to discuss in more detail the reaction scheme utilized in the present model which is based on the potential energy surface investigated by Shukla et al.<sup>54</sup>

The entrance reaction step involves the isomerization of *o*-biphenyl radical into hydrobiphenylene radical (R59 and R60). Hydrobiphenylene radical can isomerize to form monohydrocyclopenta[*a*]indene (BENZOH in Figure 2 and in Table 1) or undergo a hydrogen-loss process to biphenylene + H. Although the latter pathway (R61 and R62) is favorable from an entropic point of view, the corresponding barrier is around 7 kcal/mol higher than the barrier for the isomerization to monohydrocyclopenta[*a*]indene (R63 and R64). As also suggested by Shukla et al.,<sup>54</sup> the isomerization pathway is favorable at relatively low temperatures, as also confirmed by the low concentrations of biphenylene observed in the experiments (Figure 12). Once formed, the monohydrocyclopenta[*a*]indene intermediate can undergo a hydrogen-loss process to form cyclopenta[*a*]indene + H (R65 and R66) or proceed through a series of isomerization reactions followed by a hydrogen-loss to form acenaphthylene + H (R67). Clearly the former pathway is favorable due to the entropy contribution and due to the fact that it is constituted by a single elementary step.

Figure 15a shows the modeling results for acenaphthylene and cyclopenta[*a*]indene from the scheme described in the previous paragraph. The pathway leading to cyclopenta[*a*]indene is clearly predominant and the experimental profile for acenaphthylene is substantially underestimated. At this point it is important to underline the fact that although cyclopenta[*a*]indene was not measured in the experiments, we cannot exclude its formation just on the basis of the experimental observations since cyclopenta[*a*]indene dimerizes quickly even at room temperature. Previous studies indicate that in order to obtain NMR spectra for this species the analyses had to be run at  $-70$  °C.<sup>55,56</sup> Thus, we have to base our considerations about

cyclopenta[*a*]indene formation exclusively on the theoretical study by Shukla et al.<sup>54</sup>

The results presented in Figure 15a suggest the possibility of an isomerization pathway between cyclopenta[*a*]indene and the more stable acenaphthylene. Such pathway has experimental evidence in the work performed by Brown et al.<sup>55,56</sup> and by Wiersum and Jenneskens<sup>57</sup> on the formation of ring-contracted aromatic hydrocarbons, including acenaphthylene, starting from diradical compounds. Blake et al.<sup>58</sup> used ab initio calculations to investigate the potential energy surface for the isomerization of the biphenyl diradical into acenaphthylene through the formation of the stable cyclopenta[*a*]indene.

The results in ref 58 were used to calculate the reaction rate constants for relevant isomerization reactions. Conventional transition-state theory (TST)<sup>59–61</sup> with rigid rotor harmonic oscillator assumptions and estimated tunneling effects<sup>62</sup> was used to evaluate the high-pressure limit reaction rate constants from the quantum chemical calculations. Only the contributions from the low-frequency torsional modes, if any, were calculated using free rotor approximation. In particular, the isomerization between cyclopenta[*a*]indene and acenaphthylene was treated as a single step reaction (R80) with rate constant equal to the one for the limiting step in the global process which in reality is composed by several isomerization steps. The Arrhenius expression of the reaction rate constant calculated on the basis of the molecular properties from ref 58 is  $k_{80} \cong 2.704 \times 10^{14} \exp(-43866.5/T)$  ( $s^{-1}$ ). The modeling results obtained using such expression are reported in Figure 15b. The acenaphthylene profile is still underestimated by the model. Clearly the activation energy is too high to allow the isomerization process to occur in the temperatures range where the experimental acenaphthylene concentration starts increasing (1300–1500 K).

In order to improve the agreement between experimental and modeling profiles for acenaphthylene we derived an expression for the isomerization between cyclopenta[*a*]indene and acenaphthylene based on the experimental profiles for acenaphthylene. Such estimate is based on the assumption that acenaphthylene is mainly produced through the above-mentioned isomerization process. This assumption should be sufficiently accurate since the conventional formation pathway for acenaphthylene cannot play a significant role as discussed

earlier in the text. The expression used to evaluate the reaction rate constant is the following:

$$k = \frac{-\ln\left(\frac{[\text{BENZO}]_0 - \Delta[\text{BENZO}]}{[\text{BENZO}]_0}\right)}{t}$$

where  $[\text{BENZO}]_0$  is the initial concentration of cyclopenta[*a*]-indene as estimated by the model ignoring reaction R80,  $\Delta[\text{BENZO}] = [\text{BENZO}]_0 - [\text{BENZO}]_t \approx [\text{A2R5}]_t$ , and  $t$  is the reaction time.  $[\text{A2R5}]_t$  is the experimental concentration of acenaphthylene at time  $t$ .

The Arrhenius plot of the reaction rate constant for R80 is reported in Figure 16. The linear interpolation of the

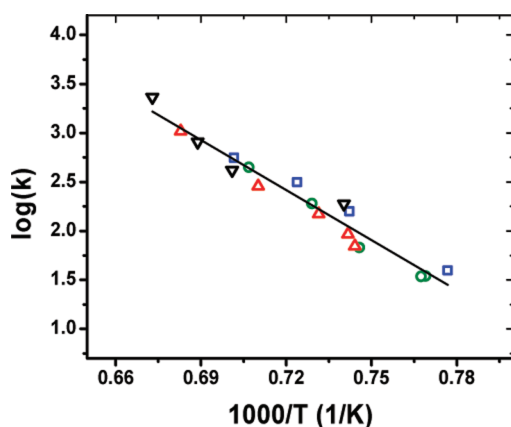


**Figure 16.** Arrhenius plot of the measured reaction rate constant for isomerization of cyclopenta[*a*]indene into acenaphthylene between 1287 and 1486 K,  $k$  in  $\text{s}^{-1}$ . Green circles,  $[\text{C}_6\text{H}_5\text{I}]_0 = 50.6$  ppm,  $p \approx 50$  atm; red triangles,  $[\text{C}_6\text{H}_5\text{I}]_0 = 95.6$  ppm,  $p \approx 50$  atm; blue squares,  $[\text{C}_6\text{H}_5\text{I}]_0 = 26.6$  ppm,  $p \approx 50$  atm; black down-triangles,  $[\text{C}_6\text{H}_5\text{I}]_0 = 54.2$  ppm,  $p \approx 25$  atm; line, linear interpolation.

experimental results provides the expression for the reaction rate constant for the isomerization of cyclopenta[*a*]indene into acenaphthylene, which is equal to  $k_{80} \approx 4.699 \times 10^{14} \exp(-39192.3/T)$ . The pre-exponential factor is slightly higher than the one obtained above from the calculations based on the results from ref 58 but within a 2-fold factor. On the other hand, the activation energy is around 9 kcal/mol lower than the theoretical one. Further theoretical calculations performed with multireference methods will clarify if the discrepancy between the theoretical and the experimental activation energies is due to inaccuracy in the theoretical methods implemented in ref 58 or to the presence of additional lower energy isomerization pathways. It is important to mention that the experimentally derived rate expression is function of the parameters of a complex model which includes among the others the estimated

reaction rate parameters for the formation of cyclopenta[*a*]-indene (R59–R67) as well as the reaction rate parameters for the formation of *o*-biphenyl radical, R27. Thus, its accuracy depends also on the accuracy of such relevant parameters in the model.

The results obtained including the experimental  $k_{80}$  expression into the model are shown in Figures 13 and 39 (Supporting Information). The formation of acenaphthylene is well reproduced by the model in terms of shape of the curve as well as mole fraction levels. In the high-temperature range of our study, above 1500 K where the experimental profiles drop, the concentrations are overestimated by the model. We can attribute this discrepancy to the absence of reaction pathways forming lighter compounds as we will discuss later in the appropriate section.

In Figures 13 and 39, the profiles of biphenylene are also reported. The simulations predict the experimental profiles accurately in the low-temperature range up to 1300 K where the formation of biphenylene is mainly driven by the recombination reaction between *o*-benzyl radicals (R58). At higher temperatures where the experimental profiles decay the modeling results do not follow the experimental trends so accurately. Above 1300 K the contribution from the isomerization reaction from hydrobiphenylene radical to biphenylene + H (R61 and R62) becomes relevant and causes the mentioned discrepancy. Thus, the experimental profiles indicate that such reaction pathway could be even less relevant than estimated. On the other hand, additional channels which consume biphenylene could be important especially in the high-temperature range of our study.

In order to test this hypothesis, a series of theoretical calculations were initiated. The model includes the results of such theoretical study performed to analyze possible biphenylene isomerization pathways (R72–R77). In particular, the study was inspired by the experimental investigations by Wiersum and Jenneskens<sup>57</sup> and by Brown et al.<sup>55,56</sup> as well as by the study by Scott<sup>63</sup> which indicate that biphenylene is a precursor of cyclopenta[*a*]indene and consequently of acenaphthylene. This possibility was investigated. The geometry optimizations and vibrational analyses were performed using the uB3LYP hybrid functional<sup>36,37</sup> with the Pople's valence triple- $\zeta$  basis set 6-311+G(d,p).<sup>38</sup> The energetics of the optimized structures were refined by single point energy calculations performed with coupled-cluster method using both single and double substitutions and including triple excitations (CCSD(T))<sup>64</sup> with Dunning's correlation consistent polarized double- $\zeta$  basis set (cc-pVDZ).<sup>65</sup> Frozen-core (FC) assumption was also used. All of the calculations were carried out with the Gaussian 03 program package.<sup>40</sup>

The results of the theoretical investigation are shown in Figure 17. The pathway identified in the present study involves the formation of a benzocyclooctatetraene-like structure

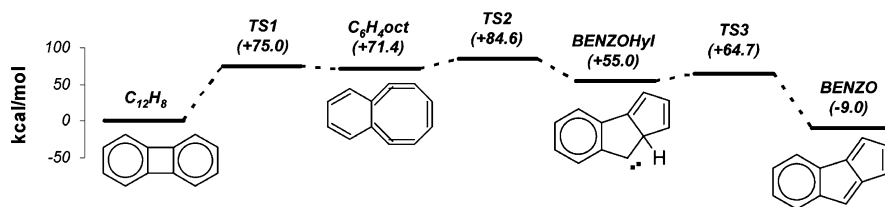


**Figure 17.** Potential energy surface for the isomerization of biphenylene into cyclopenta[*a*]indene. uB3LYP/6-311+G(d,p) optimized structures. CCSD(T)/cc-pVDZ energies in kcal/mol, including ZPVE.

(C<sub>6</sub>H<sub>4</sub>oct) (see Figure 17 for chemical structure) and subsequent reorganization to form a cyclopenta[*a*]indene-like radical (BENZOHyI) (Figure 17). Since the calculations were performed on spin-singlet structures, hydrogen-transfer processes are favorable compared to hydrogen-loss processes. As expected the BENZOHyI radical isomerizes to form cyclopenta[*a*]indene. Among the species in Figure 17 the only one which showed diradical character is BENZOHyI. The relative energy was estimated as

$$E = E(\text{CCSD(T)}) + E(\text{uB3LYP}) - E(\text{rB3LYP})$$

where  $E(\text{uB3LYP})$  and  $E(\text{rB3LYP})$  are the energies of the diradical and closed-shell compounds estimated respectively by uB3LYP/6-311+G(d,p) and rB3LYP/6-311+G(d,p) methods.

Reaction rate constants for the elementary steps involved in the isomerization process were calculated using conventional TST and rigid rotor harmonic oscillator assumptions. The rate parameters are reported in Table 1 (R72–R77). No adjustments to the reaction rate constants were made. Clearly biphenylene is a very stable compound and its dearomatization can occur only at relatively high temperatures. Only above 1500 K the contribution of the proposed pathway becomes relevant for both the consumption of biphenylene and the formation of acenaphthylene through the cyclopenta[*a*]indene intermediate. Further considerations on the necessity of further studies on the biphenylene isomerization are dependent on the accuracy of the rate parameters of the reactions involved in the formation of biphenylene as well as on the understanding of the mechanisms which leads to the formation of the light hydrocarbons that will be discussed later.

**3.1.5. Naphthalene.** The presence of fused-ring structures formed during the pyrolysis of the phenyl radical is definitely the most surprising and challenging experimental finding in the present investigation. We already discussed about the formation of acenaphthylene and its modeling. Naphthalene, the simplest among the condensed compounds, was also measured although in lower concentrations compared to acenaphthylene. The experimental profiles are shown in Figures 18 and 40

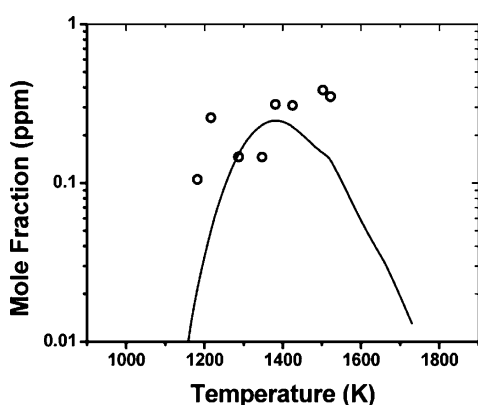


**Figure 18.** Circles, naphthalene experiments; line, naphthalene simulation.  $[\text{C}_6\text{H}_5\text{I}]_0 = 54.2 \text{ ppm}$ ,  $p \approx 25 \text{ atm}$ .

(Supporting Information). In particular, it is interesting to notice how naphthalene is produced as soon as the phenyl iodide starts decaying suggesting a link between the formation of the second-ring species and the primary products of the phenyl iodide decomposition.

Clearly the HACA mechanism<sup>1,2</sup> cannot be responsible for the experimental formation of naphthalene since acetylene is

not present in the reactant mixture or produced in large amounts at low temperatures. Comandini and Brezinsky<sup>66</sup> studied the radical/ $\pi$ -bond addition between single-ring aromatics and concluded that the reaction between *o*-benzynes and benzene leads mainly to the formation of naphthalene and acetylene through a two-step process involving the 1,4-cycloaddition between *o*-benzyne and benzene and the subsequent fragmentation of the intermediate. Similar results were reported by Shukla et al.<sup>54</sup> Both benzene and *o*-benzyne are formed as primary products of the decomposition of the phenyl iodide and reaction between phenyl radicals, thus the proposed pathway was included in the model (R149–R151). The reaction rate constant  $k_{150}$  was calculated on the basis of the structures and energetics provided in ref 66 using conventional TST. In addition the reaction rate constant for the entrance reaction, the 1,4-cycloaddition, was multiplied by a factor of 2 within the uncertainty provided by the authors. For consistency  $k_{150}$  was also multiplied by a 2-fold factor.

The results of the simulations are reported in Figures 18 and 40, and show an excellent agreement with the experiments not only in terms of profile shape but also in terms of concentrations. The experimental results confirm the relevance of the radical/ $\pi$ -bond addition between *o*-benzyne and benzene as source of the second-ring species in this kind of pyrolytic systems.

**3.1.6. Four-Ring Compounds.** Even more surprising than the formation of acenaphthylene and naphthalene was the identification and measurement of a variety of four-ring fused compounds including chrysene, triphenylene, benzo[*a*]anthracene, benzo[*g,h,i*]fluoranthene, and benzo[*c*]phenanthrene. An example of the profiles for these species is shown in Figure 19 for the experimental set conducted at a nominal pressure of 50 atm with an initial phenyl iodide mole fraction equal to 95.6 ppm for which the mole fractions of the four-ring compounds are maximum. The experimental profiles provide critical information on how these large compounds could be formed.

First of all it is important to notice that chrysene and triphenylene coelute in the present analytical setup. In fact, it is not possible to separate these two compounds using a (50%-Phenyl)-methylpolysiloxane phase column as the DB-17ms.<sup>67</sup> The LC-50 column, dimethyl-(50% Liquid Crystal), is not suitable for measuring the lighter PAH species, but it provides a good separation of heavy isomers, as for example triphenylene and chrysene. A series of relevant experiments were conducted with a LC-50 column attached to the second FID detector in parallel with the DB-17ms column, so that heavy species could be separated through the two different columns for better resolution. The results indicated that the peak area measured with the DB-17ms is constituted by 90% of chrysene and 10% of triphenylene. With this in mind, we can clearly state that the major four-ring compound produced in the pyrolysis of phenyl radical is chrysene. Only small amounts of the other isomers are produced.

Even more important from a mechanistic point of view is the fact that the chrysene is formed as soon as phenyl iodide starts decomposing. Conventional pathways for the formation of this compound include the HACA mechanism starting from phenanthrene. Since phenanthrene is only measured in trace amounts in the experiments and acetylene is not produced at low temperatures, the HACA mechanism cannot be responsible for the formation of chrysene. Thus, such species must be produced by some sort of recombination between three single-

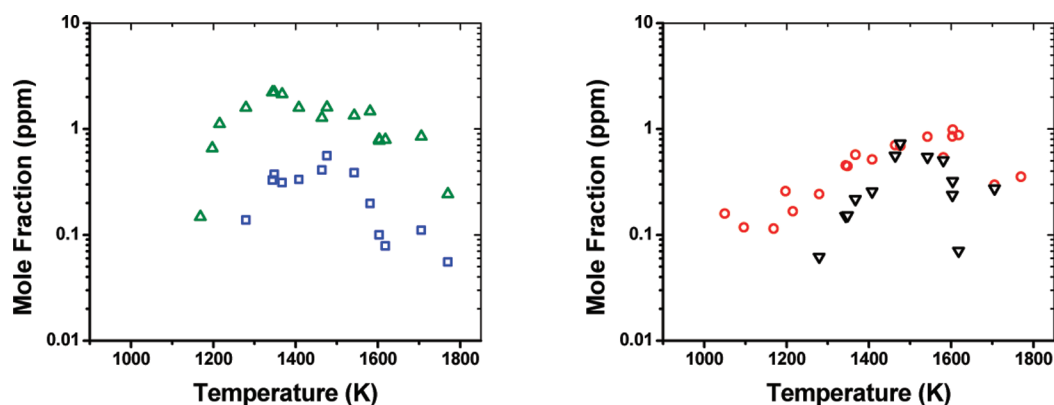


**Figure 19.** Experimental mole fraction,  $[C_6H_5I]_0 = 95.6$  ppm,  $p \approx 50$  atm. Green triangles, chrysene ( $\sim 90\%$ ) + triphenylene ( $\sim 10\%$ ); blue squares, benzo[*a*]anthracene; red circles, benzo[*g,h,i*]fluoranthene; black down-triangles, benzo[*c*]phenanthrene.

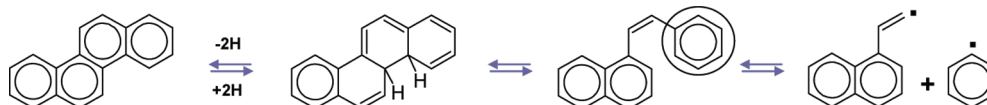


**Figure 20.** Deconstruction of the molecular structure of chrysene.

ring aromatic compounds. On the other hand, benzo[*a*]anthracene, benzo[*g,h,i*]fluoranthene, and benzo[*c*]phenanthrene are formed at higher temperatures, indicating that these isomers could derive from the isomerization of chrysene.

In order to understand the mechanisms of formation of chrysene, we deconstructed its molecular structure into simpler components. The only reasonable pathway we were able to identify is the one reported in Figure 20. The primary reactants on the right of the figure are naphthyl vinyl radical and phenyl radical which can recombine to form an intermediate compound which undergoes ring closure and dehydrogenation to chrysene. This process is a sort of PAC mechanism of the naphthyl vinyl radical. The main problem with the proposed pathway is the fact that the naphthyl vinyl radical once formed would isomerize quickly to form acenaphthylene<sup>52</sup> and would not be available for the recombination reaction with the phenyl radical. A different mechanism must be responsible for the formation of chrysene.

Shukla and Koshi<sup>13,14</sup> identified the presence of triphenylene in their experimental work on benzene pyrolysis. Thus, we can hypothesize that triphenylene is produced as the primary four-ring compound in our experiments too and that it subsequently undergoes isomerization to form chrysene. Since such an isomerization process is unknown, from a modeling point of view we will consider only the formation of triphenylene and compare the modeling results with the sum of the experimental mole fractions of all the four-ring species (Figures 21 and 41, Supporting Information). The correspondence between the calculated triphenylene concentrations and the measured concentrations provides an estimate of the accuracy of the reaction pathways in the model keeping in mind the fact that triphenylene subsequently undergoes isomerization into chrysene and at higher temperatures into benzo[*a*]anthracene, benzo[*g,h,i*]fluoranthene, and benzo[*c*]phenanthrene too.

The formation of triphenylene is the prototype of the PAC mechanism;<sup>13,14</sup> Shukla and Koshi hypothesized that phenyl adds to biphenyl to form *o*-terphenyl which subsequently undergoes cyclodehydrogenation process to triphenylene.

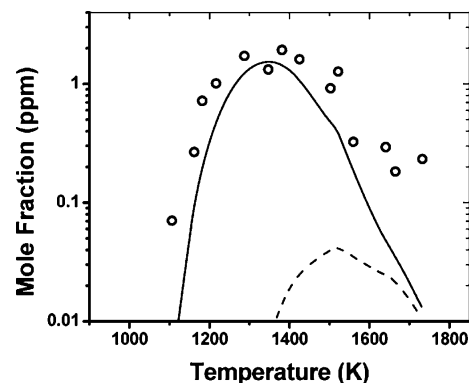


**Figure 21.** Circles, sum of four-ring compounds experiments; solid line, triphenylene, model in Table 1; dashed line, triphenylene, model in Table 1 omitting R57.  $[C_6H_5I]_0 = 54.2$  ppm,  $p \approx 25$  atm.

The latter step has always been controversial. Experimental studies on benzene pyrolysis<sup>68</sup> and on biphenylene pyrolysis<sup>69</sup> indicate that the cyclodehydrogenation process does not occur, although studies supporting the contrary are present in literature.<sup>50,70</sup> We will try to use our experimental results to clarify the point.

We have already discussed the formation of *o*-terphenyl (section 3.1.3) and mentioned that from a modeling point of view its cyclodehydrogenation is energetically unfavorable due to its high activation energy (84.7 kcal/mol, R55). This consideration is based on estimated parameters which may not be very accurate, so we need to find a more convincing justification to rule out the cyclodehydrogenation process. Such justification derives from a simple empirical observation. The amount of *o*-terphenyl produced in the system (Figures 11b and 38, Supporting Information) is not sufficient to justify the high mole fractions of four-ring compounds observed in the experiments even if *o*-terphenyl were entirely converted into triphenylene. Thus, a different mechanism must be involved in the formation of the four-ring compounds.

Fields and Meyerson<sup>71,72</sup> reported the measurement of triphenylene in their pyrolytic studies on the reaction between



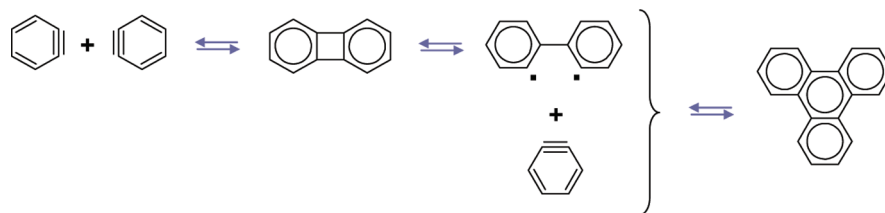


Figure 22. *o*-Benzynes trimerization pathway.

*o*-benzynes and benzene. The authors hypothesized that the formation of triphenylene is mainly due to trimerization of *o*-benzynes radicals. Lindow and Friedman<sup>69,73</sup> investigated the liquid and vapor-phase pyrolysis of biphenylene and based on the distribution of the product species concluded that a relatively high concentration of the diradical species in Figure 22 is present especially in the high-temperature range of their experiments (730 °C). Such diradical can react with *o*-benzynes and form triphenylene as shown in Figure 22. An important consideration reported by Lindow and Friedman is that naphthalene is not produced even when the experiments are conducted in benzene for which the estimated barrier is less than 7 kcal/mol.<sup>66</sup> This indicates that the reaction between the diradical intermediate and the *o*-benzynes radical must be very fast in order to justify the fact that all the *o*-benzynes radicals are consumed by the pathway in Figure 22 even when large concentrations of benzene are present. In order to account for such favorable trimerization process, we assumed that *o*-benzynes reacts directly with biphenylene (R57) with a reaction rate constant similar to the one used for the dimerization of *o*-benzynes radicals (R58).

The results of the simulations are reported in Figures 21 and 41 (Supporting Information). The modeling profiles are in excellent agreement with the experiments not only for the general shape but also in terms of maximum mole fractions of the product species. This indicates that the proposed pathway is most likely correct, although we need also to take into account the large uncertainty in the quantification of the four-ring species before drawing a conclusion on the accuracy of the estimated reaction constant  $k_{57}$ . For comparison the modeling results using only the PAC mechanism are also shown (dashed lines). The results confirm the hypothesis that the PAC mechanism is not adequate to explain the formation of the four-ring compounds in the system in consideration.

Before concluding this section, we would like to mention that the diradical intermediate in Figure 22 can dimerize as shown in the previous studies on the biphenylene pyrolysis.<sup>69,73</sup> This process could be responsible for the discrepancy between experimental and modeling profiles for biphenylene reported in the corresponding section and in Figure 13. Such hypothesis requires additional theoretical validations.

**3.1.7. Light Hydrocarbons.** Although the main focus of the present investigation is to study the formation of PAHs and the relevance of the chemical mechanisms involved, several light hydrocarbons were measured, including the major products benzene, acetylene, diacetylene, and triacetylene. Benzene formation has been already discussed earlier in the text in the corresponding section and no additional analyses are necessary for the purpose of the present investigation. The main consideration we need to keep in mind about the discussion on benzene is the fact that although the low-temperature profiles are well reproduced by the model, the benzene concentrations in the high-temperature range of our study are

overestimated by the model (Figure 7). Overestimation of the experimental profiles at high temperatures has been also observed for other product species, i.e., biphenyl (Figure 7), biphenylene, and acenaphthylene (Figure 13). Of course this means that the formation of other experimental compounds is underestimated. However before considering the modeling results we start as usual with the analysis of the experimental profiles of the remaining major compounds, i.e., acetylene, diacetylene, and triacetylene.

As expected, the formation of acetylene and polyacetylenes occurs in the high-temperature range of our study mainly above 1400 K. Wang et al.<sup>74</sup> investigated the decomposition of the phenyl radical using ab initio calculations and concluded that it proceeds through C–H fission to form *o*-benzynes (R161) which subsequently undergoes fragmentation into acetylene and diacetylene (R163). The derived reaction rate constants were included in the model used by the authors to accurately simulate the decomposition of benzene in shock-tube experiments where the polyacetylenes were measured.<sup>76</sup> Based on the mechanism proposed by Wang et al.,<sup>74</sup> the formation of acetylene and diacetylene are strictly coupled and the corresponding concentrations should be very similar at least at low temperatures. As shown in Figures 23 and 42 (Supporting Information), the experimental profiles from the present study do not follow the expected behavior.

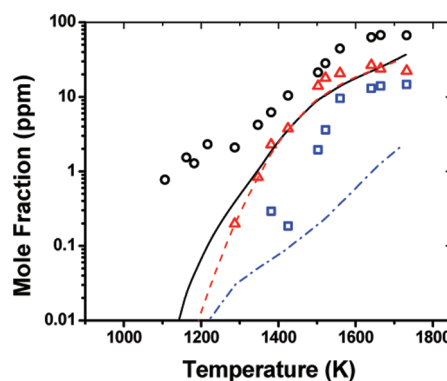


Figure 23. Black circles, acetylene experiments; black line, acetylene simulation; red triangles, diacetylene experiments; red dashed line, diacetylene simulation; blue squares, triacetylene experiments; blue dash-dotted line, triacetylene simulation.  $[C_6H_5I]_0 = 54.2$  ppm,  $p \approx 25$  atm.

The first obvious discrepancy between the experimental and the expected trends consists in the fact that acetylene is produced in much larger concentrations compared to diacetylene even at the relatively low temperatures when the profiles starts to increase rapidly (1400 K). The second less evident difference between the acetylene and the diacetylene profiles is that acetylene is produced also below 1400 K, although in small amounts (few ppm). This evidence suggests

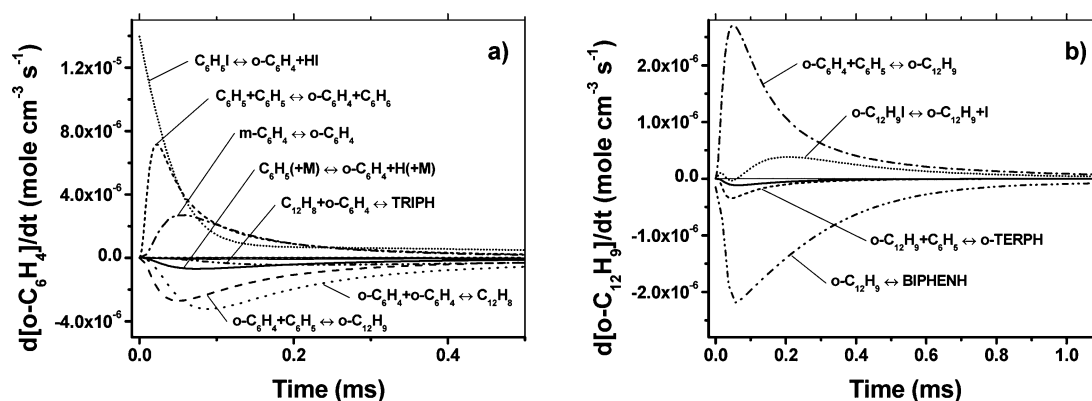


Figure 24. Rate of production analysis,  $[C_6H_5I]_0 = 54.2$  ppm,  $T = 1287$  K,  $p = 28.3$  atm: (a) *o*-benzyne radical and (b) *o*-biphenyl radical.

that there could be an additional low-energy reaction pathway which favors the formation of acetylene. The comparison between the experimental profiles for acetylene and diacetylene and the modeling results confirm such hypothesis (Figures 23 and 42). In fact, although the modeling profiles start increasing around 1400 K as the experiments indicate, the *o*-benzyne fragmentation pathway is not sufficient to justify the steep increase in the experimental mole fractions especially of acetylene. In addition the experimental profiles reach a sort of equilibrium at relatively low temperatures, around 1700 K for acetylene and 1600 K for diacetylene, while the modeling profiles do not reproduce such behavior. Finally no formation of acetylene is predicted at temperatures below 1400 K indicating that the model is not complete.

Different considerations apply for triacetylene. The corresponding experimental profiles have a similar trend to the profiles of acetylene and diacetylene with a relatively steep increase starting around 1450 K before reaching the equilibrium value around 1700 K. Of course the mole fractions of triacetylene are lower than the ones of acetylene and diacetylene. This is in agreement with the hypothesis that triacetylene could be mainly formed through polymerization.

The polymerization steps are included into the model but constitute only a minor pathway for the formation of triacetylene. Reaction pathway analysis indicates that triacetylene is mainly produced through decomposition of the  $C_6H_3$  radical (reverse of R166, ref 77) which is formed principally by reaction R171,  $z-C_6H_4 + H \leftrightarrow C_6H_3 + H_2$  (ref 32). As already discussed,  $z-C_6H_4$  is the product of the Bergman decyclization of *p*-benzyne (R26). As shown in Figures 23 and 42, the model significantly underestimates the concentrations of triacetylene. In particular, the polymerization mechanism should play a more relevant role for the formation of such polyacetylene as we will also discuss in the second part of the article in relation to the phenyl + acetylene reaction.

The results reported in the present section indicate that although the formation of the PAH products is well simulated by the model, additional work is required in order to reach a similar accuracy with respect to the profiles of the light hydrocarbon compounds. On the other hand, the experimental results provide a very important benchmark for further development of the chemical kinetic model and for testing novel reaction pathways in particular in relation to the formation of acetylene. Possible pathways could involve the direct fragmentation of the large PAH compounds into small aliphatic hydrocarbons. A key role could be played by the presence of hydrogen atoms which could quite easily add to the

various sites available in PAH compounds and allow access to alternative potential surfaces. Recent investigations have demonstrated how H-addition reactions are able to initiate PAH growth pathways lower in energy than those initiated by H-abstraction reactions.<sup>78–80</sup> Similarly, low energy pathways initiated by H-addition could exist for the fragmentation of the PAH intermediates at the high-pressure conditions of the present investigation. This possibility clearly requires further theoretical validations.

**3.1.8. PAC, Benzyne Chemistry, and Polymerization.** Now that we have presented a complete analysis of the experimental and modeling results on the pyrolytic reactions of the phenyl radical, we summarize the main findings in view of the initial purpose of the investigation, i.e., clarifying the role of the relevant reaction mechanisms. The considerations reported in this section apply specifically to the primary growth reaction steps up to the formation of the four-ring compounds. However, much of the present discussion can be extended to systems which involve reactions between even larger compounds.

First, the experimental and modeling results indicate that for the system under consideration the PAC mechanism is not enough. In particular, the cyclization of *o*-terphenyl is energetically unfavorable in the temperature range of this study, and the PAC mechanism alone is not sufficient to account for the formation of the large four-ring PAH compounds.

On the other hand, it is clear from the entire prior discussion that the presence of the benzyne enhances the formation of almost all the PAH compounds measured in the present investigation. While the *p*-benzyne undergoes rapid isomerization into 1,5-hexadiyn-3-ene (Bergman decyclization R26) and does not contribute to the growth process, the *m*-benzyne is the primary factor in the formation of the *m*-terphenyl. In fact, it recombines with phenyl radicals to form *m*- $C_{12}H_9$  radicals (R28) which constitute the primary building block for the formation of the *m*-terphenyl through reaction R50. Nevertheless we focus our attention on the chemistry associated with the *o*-benzyne radical, the most abundant among the benzyne isomers and definitely the most influential intermediate in relation to PAHs formation.

*o*-Benzyne is mainly produced by three reaction pathways as shown in Figure 24a, i.e., the decomposition of phenyl iodide into *o*-benzyne and HI (R3), the H-abstraction between phenyl radicals (R21), and the isomerization of *m*-benzyne (R24). Once formed, *o*-benzyne reacts with the most abundant radical intermediates present in the system, i.e., *o*-benzyne to form

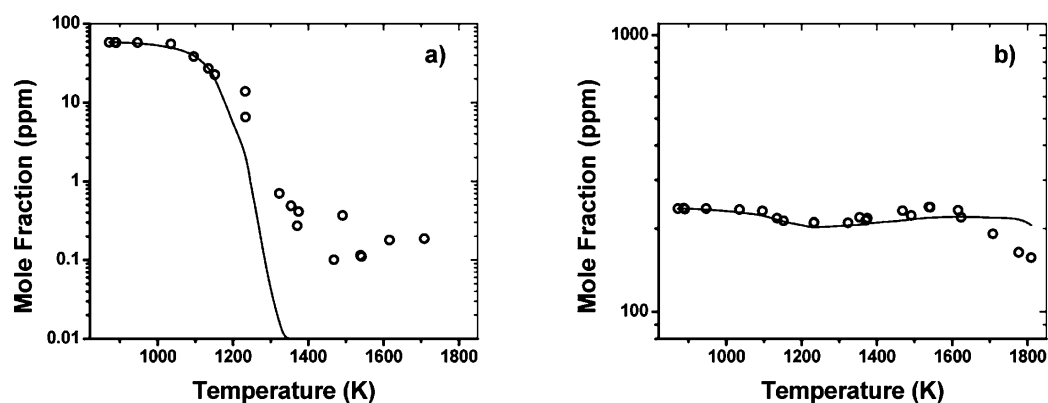


**Figure 25.** (a) Circles, phenyl iodide experiments; line, phenyl iodide simulation. (b) Circles, acetylene experiments; line, acetylene simulation.  $[\text{C}_6\text{H}_5\text{I}]_0 = 58.1$  ppm,  $[\text{C}_2\text{H}_2]_0 = 236.3$  ppm,  $p \approx 50$  atm.

biphenylene (R58) and phenyl to form  $o\text{-C}_{12}\text{H}_9$  (R27). In particular,  $o$ -biphenyl radical is a very important intermediate for the formation of PAH compounds as indicated in Figure 24b. In fact, in addition to constituting the primary building block for the formation of  $o$ -terphenyl (R49) it can easily isomerize into the hydrobiphenylene radical (R59) which is the precursor for the formation of cyclopenta[*a*]indene, acenaphthylene, and biphenylene - to a minor extent. The reaction rate analysis in Figure 24b confirms that  $o\text{-C}_{12}\text{H}_9$  is mainly formed by reaction between  $o$ -benzyl and phenyl radical. Moreover,  $o$ -benzyl is also responsible for the formation of naphthalene through cycloaddition with benzene and subsequent fragmentation of the intermediate (R149–R151) and possibly for the formation of triphenylene through trimerization (R57).

The results summarized above not only highlight the importance of the  $o$ -benzyl chemistry for the formation of a variety of PAH components relevant to the formation of soot, but also draw attention to a wider category of compounds, the diradicals. In particular, at high-temperatures where the dehydrogenation or H-abstraction processes play a significant role the presence of relatively high concentrations of diradical species could drive the growth to larger PAH compounds by cycloaddition or even more rapidly by diradical-diradical recombination. Clearly these processes would be in competition with the conventional growth mechanisms, i.e., the HACA mechanism or the PAC mechanism.

A final note regarding the formation of acetylene at relatively high temperatures and the consequent polymerization process: the experimental profiles indicate that below 1300–1400 K the formation of PAH compounds is the predominant pattern. All the PAHs but acenaphthylene have the highest concentrations in this temperature range after which the profiles drop. Above 1400 K the formation of acetylene becomes predominant together with the polymerization process to form the polyacetylenes. Further investigations are required in order to clarify the high-temperature mechanisms responsible from a theoretical point of view.

**3.2. Phenyl + Acetylene Reaction.** Now that the mechanisms which lead to the formation of PAH compounds from the pyrolysis of the phenyl radical have been studied in details both experimentally and theoretically we can move to the second part of our investigation which regards the reaction between the phenyl radical and acetylene. Just as for the phenyl pyrolysis study, we will present the major experimental and modeling results with particular attention to the specific mechanisms involved in the formation of the PAH products.

The experimental and modeling results at 25 atm are very similar to the results obtained at 50 atm with higher acetylene concentrations and thus are not shown. The graphs containing the experimental and modeling results obtained with a smaller or larger amount of acetylene have been included respectively in the article and in the Supporting Information. It is worth mentioning that although not discussed in details, trace amounts of several other PAH compounds were detected, including most of the compounds shown in Figure 3. However, the pathways characteristic of the phenyl pyrolysis now play only a minor role.

**3.2.1. Phenyl Iodide Decomposition and Acetylene Profiles.** The mechanisms of decomposition of the phenyl radical precursor phenyl iodide are of course similar to the ones described for the phenyl pyrolysis study. The only major difference is the presence of hydrogen atoms in the system from the reaction between phenyl radical and acetylene to form phenylacetylene and H. The free hydrogen atoms can react with the phenyl iodide and abstract the iodine atom (reaction R4 in Table 1). This reaction was studied both experimentally and theoretically by Gao et al.<sup>81</sup> and the reaction rate constant derived by the authors was used in the present model within the given uncertainty limits. The experimental and modeling profiles for phenyl iodide are reported in Figures 25a and 43 (Supporting Information). Good agreement between experiments and simulations was obtained.

In these experimental sets, acetylene is also added as a reactant to the initial mixture. As we can observe in Figures 25b and 44 (Supporting Information), the acetylene profiles show similar trends for all sets. The trends are characterized by a drop in correspondence with the decay of the phenyl iodide, a recovery above 1300 K before a more consistent drop at higher temperatures (above around 1600 K). The model accurately predicts the experimental behavior of the acetylene profiles with regards to both the shape of the profiles and the concentrations. Clearly this indicates that the chemistry involved in the formation and consumption of acetylene is well represented by the model. Only at high temperatures does the model overestimate the experimental mole fractions. We will discuss the reason for such a discrepancy in the section related to the polyacetylenes (section 3.2.6).

**3.2.2. Phenylacetylene and Benzene.** Phenylacetylene is obviously the major product from the reaction between the phenyl radical and acetylene. The reaction proceeds through formation of the phenylvinyl radical ( $\text{C}_6\text{H}_5\text{CHCH}$ ) and a subsequent hydrogen-loss step to form phenylacetylene and

hydrogen (R90 and R91). The reaction rate constants for R90 and R91 utilized in the present work were obtained by Tokmakov and Lin<sup>22</sup> using quantum chemical calculations and transition state theory. In particular, the reaction rate constant for reaction R90 was reduced by a factor of 2 compared to their calculated value. This modification was necessary in order to improve the agreement between the simulation results obtained using R90 and R91 with the results obtained by replacing the two step process with the global reaction  $C_6H_5 + C_2H_2 \leftrightarrow C_8H_6 + H$  using a reaction rate constant derived experimentally by Heckmann et al.<sup>15</sup>

At low temperatures the process is mainly limited by the concentration of phenyl radicals in the system as indicated in Figure 26, where the experimental profiles for phenylacetylene

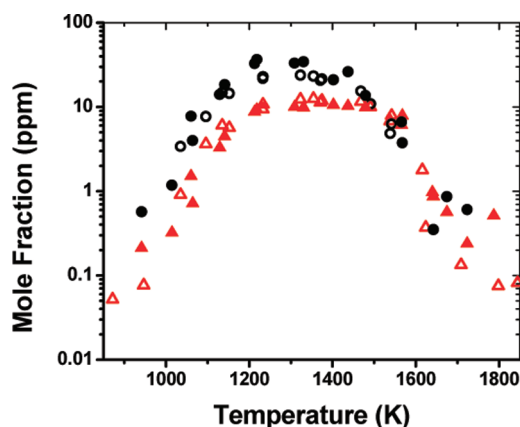


**Figure 26.** Experiments,  $p \approx 50$  atm. Black open circles, phenylacetylene,  $[C_6H_5I]_0 = 58.1$  ppm,  $[C_2H_2]_0 = 236.3$  ppm; red open triangles, benzene,  $[C_6H_5I]_0 = 58.1$  ppm,  $[C_2H_2]_0 = 236.3$  ppm; black solid circles, phenylacetylene,  $[C_6H_5I]_0 = 55.1$  ppm,  $[C_2H_2]_0 = 511.3$  ppm; red solid triangles, benzene,  $[C_6H_5I]_0 = 55.1$  ppm,  $[C_2H_2]_0 = 511.3$  ppm.

are reported for the two sets conducted at a nominal pressure of 50 atm and with different initial amounts of acetylene (236.3 and 511.3 ppm). In fact, the initial slope for the formation of phenylacetylene is similar in both cases independently of the  $C_2H_2$  mole fraction. Above 1175 K the experimental profiles start diverging and in the temperature range where the phenylacetylene profiles reach the maximum value (around 1275 K) the ratio between the phenylacetylene mole fractions is around 0.69, higher compared to the ratio between the acetylene concentrations (around 0.46). Thus, although the initial acetylene mole fraction does have an influence on the formation of phenylacetylene, the initial mole fraction of phenyl iodide is a limiting factor even at intermediate temperatures.

On the other hand, the experimental profiles for benzene indicate that the formation of this product is almost entirely dependent on the initial phenyl iodide concentration. In fact, as shown in Figure 26, the initial acetylene mole fraction does not have an influence on the concentration of benzene produced along the entire temperature range of our study. This is a clear indication that the pathways for the formation of benzene are very efficient and involve reactions with very reactive compounds. This is indeed the case. As shown in Figure 27, the reactions responsible for the formation of benzene are the recombination between phenyl and H (R44) and the reaction between phenyl and HI (R5). The main difference with the experiments conducted without acetylene is the relevance of

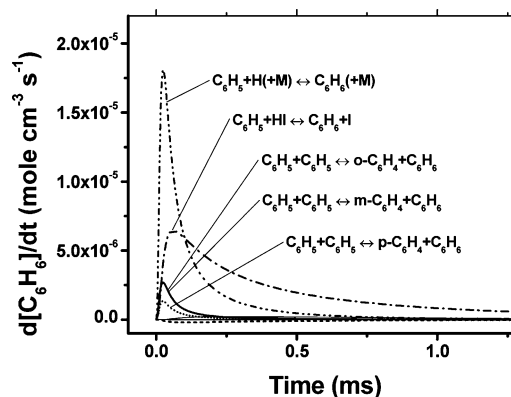


**Figure 27.** Analysis of the rate of benzene production.  $[C_6H_5I]_0 = 58.1$  ppm,  $[C_2H_2]_0 = 236.3$  ppm,  $T = 1233$  K,  $p = 47.1$  atm.

reaction R44 even at low temperatures due to the presence of large concentrations of H atoms from reaction R91. Reaction R5 still has a major influence on the ability to model the benzene formation. On the other hand, the H-abstraction channel between phenyl radicals (R21–R23) has a minor role due to the fact that the phenyl radicals are removed by the efficient reaction with acetylene and not available for self-reaction.

The results of the simulations are reported in Figures 28a and 45 (Supporting Information). The model reproduces correctly the formation of both species for temperatures up to 1300 K. At higher temperatures, especially above 1400 K, the concentrations of benzene and phenylacetylene are overestimated. This behavior is similar to what we observed in the modeling results of the major species of the study on the phenyl pyrolysis. We can attribute this discrepancy to the same reason hypothesized in the first part of the article: that the model does not include relevant pathways which consume the intermediates forming smaller compounds, i.e., the polyacetylenes.

**3.2.3. Diphenylethyne and Phenanthrene.** If we compare the distribution of PAH products in the phenyl + acetylene system with the one observed for the phenyl pyrolysis study we would be surprised that not many additional product peaks were measured. The major difference in adding acetylene as an initial reactant consists in the presence of the C14 compounds, i.e., diphenylethyne and phenanthrene. The experimental profiles of these compounds are reported in Figures 28b and 46 (Supporting Information). The experiments indicate that the formation of diphenylethyne is slightly faster than the one of phenanthrene in the low-temperature range of our study. In addition diphenylethyne concentrations reach slightly higher values compared to phenanthrene before decaying above 1250–1300 K.

The mechanisms of formation for phenanthrene are quite well known. The first relevant mechanism involves the reaction between *o*-biphenyl radical and acetylene, forming phenanthrene + H (R100).<sup>82</sup> At low temperature such reaction provides only a minor contribution to the formation of phenanthrene for the case in consideration. In fact, the major contribution derives from the reaction between phenyl radical and phenylacetylene.<sup>83</sup> Such reaction has been investigated by Iparraguirre and Kloppe<sup>84</sup> using ab initio calculations but due to the complexity of the study we preferred to use for modeling purposes an estimated global reaction rate constant (R101) based on the model presented in ref 33.



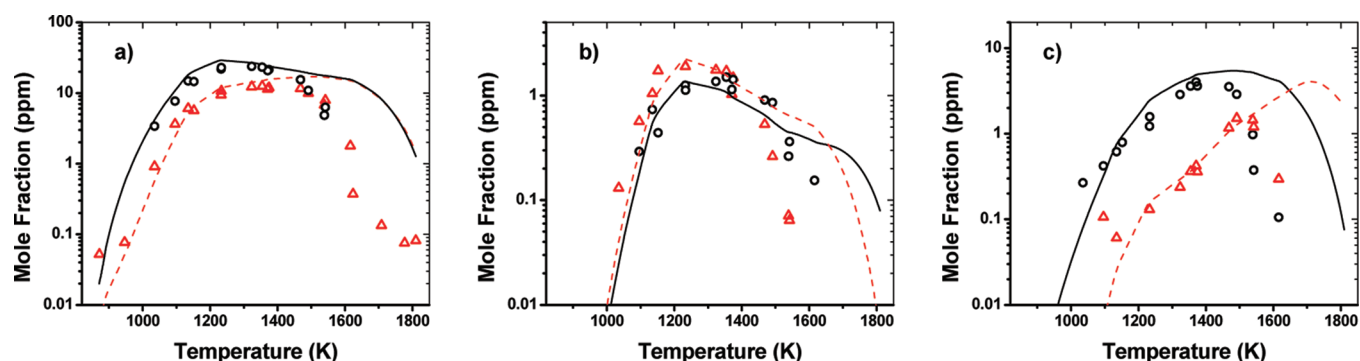


**Figure 28.** (a) Black circles, phenylacetylene experiments; black line, phenylacetylene simulation; red triangles, benzene experiments; red dashed line, benzene simulation. (b) Black circles, phenanthrene experiments; black line, phenanthrene simulation; red triangles, diphenylethyne experiments; red dashed line, diphenylethyne simulation. (c) Black circles, biphenyl experiments; black line, biphenyl simulation; red triangles, acenaphthylene experiments; red dashed line, acenaphthylene simulation.  $[C_6H_5I]_0 = 58.1$  ppm,  $[C_2H_2]_0 = 236.3$  ppm,  $p \approx 50$  atm.

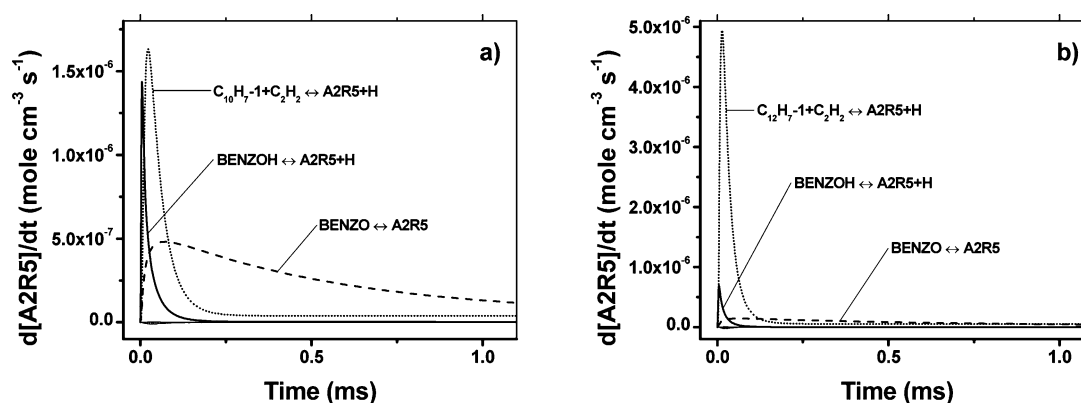


**Figure 29.** Analysis of the rate of acenaphthylene production. (a)  $[C_6H_5I]_0 = 58.1$  ppm,  $[C_2H_2]_0 = 236.3$  ppm,  $T = 1491$  K,  $p = 50.3$  atm. (b)  $[C_6H_5I]_0 = 55.1$  ppm,  $[C_2H_2]_0 = 511.3$  ppm,  $T = 1479$  K,  $p = 51.1$  atm.

On the other hand, to the best of our knowledge, no previous studies have considered the formation of diphenylethyne, although the potential energy surface proposed in ref 84 contains intermediate structures which could be precursors for diphenylethyne. In view of the structure of diphenylethyne and the system in consideration, finding the pathway for its formation becomes trivial. Clearly diphenylethyne is formed through addition between phenyl radical and phenylacetylene with subsequent hydrogen loss in a similar fashion as the reaction between  $C_6H_5$  and  $C_2H_2$  forming phenylacetylene + H. This is the reason why we considered the same reaction rate constant for both processes ( $k_{98}$  equal to the experimental rate constant from 15). The reaction rate constant for the reverse reaction (R99) was estimated on the basis of the results by Hertzler and Frank<sup>85</sup> on the reaction between phenylacetylene and H. In particular, the pre-exponential factor was multiplied by a factor of 2 due to the multiplicity of the reaction pathway.

The results of the simulations show excellent agreement with the experiments especially for the profiles of diphenylethyne (Figures 28b and 46). The formation of phenanthrene at low temperatures is also well simulated by the model indicating that the corresponding reaction rate parameters in the model are appropriate. In particular, it is worth highlighting that the relative formation slopes are well reproduced. The major discrepancy between experiments and simulations consists in the fact that the phenanthrene experimental profiles obtained with higher  $C_2H_2$  mole fractions reach higher concentrations than the modeling profiles. This is a consequence of the fact

that the modeling profiles reach the maximum at around 1250 K in correspondence with the maximum  $C_6H_5C_2H$  values while the maximum experimental value is obtained at higher temperatures (around 1350 K). Different alternative pathways for the formation of phenanthrene were considered including the Diels–Alder mechanism between biphenyl and acetylene studied by Kislov et al. (R112 and R113, ref 86). No improvement in the modeling results could be obtained.

**3.2.4. Biphenyl and Acenaphthylene.** The mechanisms of formation of biphenyl and acenaphthylene have been described in detail in the first part of the article since both are produced in large concentrations by the pyrolytic reactions of the phenyl radical. The two C12 compounds are present also when acetylene is added in the initial mixture, although in lower amounts as shown in Figures 28c and 47 (Supporting Information). In particular, biphenyl formation is significantly reduced due to the fact that phenyl radicals are removed by the reaction with acetylene and thus are not available for self-recombination.

A similar consideration applies for acenaphthylene, although in this case the reduction is not as substantial as expected due to the fact that the HACA mechanism provides a significant contribution to the production of the species (R94 + R153 + R81). The relevance of the HACA mechanism of course depends on the initial concentration of acetylene. Figure 29 shows the results of the rate of production analyses for acenaphthylene conducted at similar temperature and pressure conditions but for different initial acetylene mole fractions.

While the results in Figure 29a indicate that in the system with an initial acetylene concentration of 236.3 ppm the HACA mechanism competes with the alternative formation pathways which were found to be significant in the study conducted without acetylene, an increase in the acetylene concentration enhances the relevance of the HACA pathway (Figure 29b). In the latter case the HACA mechanism clearly dominates the acenaphthylene formation processes.

The modeling profiles are reported in Figures 28c and 47. The experimental profiles of biphenyl are well simulated by the model, although overestimated at temperatures higher than 1400 K. The formation of acenaphthylene is also accurately predicted up to around 1500 K which confirms the accuracy of the reaction pathways considered in the present work. At higher temperatures the experimental profiles drop rapidly while the simulated mole fractions increase up to 1725 K before decaying. This is another confirmation of the fact that the model is not complete but should include additional pathways which lead for example to the formation of light compounds.

**3.2.5. Naphthalene.** The analysis performed on acenaphthylene indicates that the HACA mechanism has a major role in the formation of such a compound. As is well known, one of the elementary steps of the HACA mechanism involves the formation of the naphthyl radical through reaction R153. Naphthyl radical could react with hydrogen atoms and lead to the formation of the second-ring species (R155). In addition, the stabilization of the phenylvinyl radical (R90) and the migration of its radical site to the ring (R92)<sup>87,22</sup> could open a parallel pathway to naphthalene through the addition of a second  $C_2H_2$  molecule and ring closure to form naphthalene (R152). Pathways initiated by hydrogen migration have been suggested as relevant to the formation of a variety of large PAH intermediates.<sup>88</sup> Thus, it is interesting to understand if for the system under consideration naphthalene is produced in substantial amounts and how the formation of naphthalene compares with the results of the phenyl pyrolysis study (Figure 18).

The experimental results clearly show that the pathways previously identified as leading to naphthalene do not play a significant role at the conditions implemented in the present investigation (Figures 30 and 48, Supporting Information). The amounts of naphthalene produced are indeed comparable with the ones observed in Figure 18. On the other hand, the profiles in Figures 30 and 48 have a very peculiar trend typical of a bimodal formation process. At least from a qualitative point of

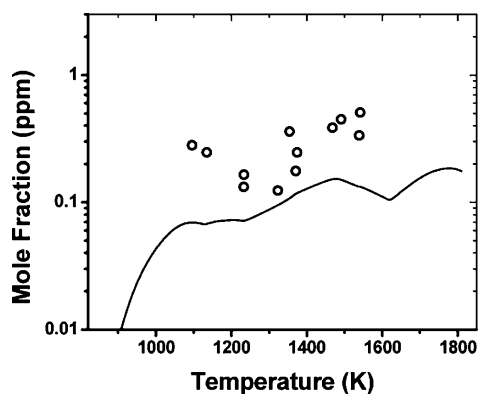


**Figure 30.** Circles, naphthalene experiments; line, naphthalene simulation.  $[C_6H_5I]_0 = 58.1$  ppm,  $[C_2H_2]_0 = 236.3$  ppm,  $p \approx 50$  atm.

view the model reproduces the bimodal behavior also in relation to the simulation of the temperatures at which the experimental peaks occur.

Based on the rate of production analysis conducted at  $\sim 1060$  K (50 atm nominal pressure, initial acetylene mole fraction of 511.3 ppm), the formation of naphthalene at low temperatures occurs almost entirely through reaction R152. Thus, the mechanism involving the hydrogen migration in the phenylvinyl structure followed by  $C_2H_2$  addition and cyclization plays an important role at relatively low temperatures (below 1250 K). On the other hand, at higher temperatures the phenylvinyl radical quickly undergoes hydrogen loss to form phenylacetylene. At around 1480 K the rate of production analysis indicates that the dominant pathway to naphthalene involves the cycloaddition reaction between benzene and *o*-benzynes and the subsequent fragmentation of the resulting bicyclo intermediate.<sup>66</sup> This pathway is responsible for the formation of naphthalene from phenyl radical pyrolysis as discussed in section 3.1.5. Although to a minor extent, the conventional HACA mechanism contributes to the formation of naphthalene at 1480 K. The relatively low importance of the HACA mechanism is attributable to the fact that the naphthyl radicals produced through the HACA mechanisms are mainly consumed by reaction with acetylene to form acenaphthylene and are not available for recombination with H atoms to form naphthalene.

**3.2.6. Polyacetylenes.** Similarly to what we observed in the study on the phenyl pyrolysis, in the high-temperature range of the present investigation the polyacetylenes become the main products while the PAH compounds are consumed. Figure 31

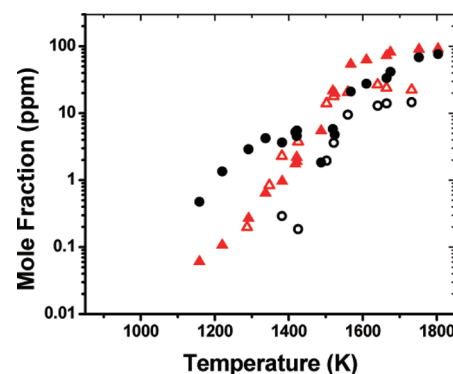


**Figure 31.** Experiments,  $p \approx 25$  atm. Black open circles, triacetylene,  $[C_6H_5I]_0 = 54.2$  ppm; red open triangles, diacetylene,  $[C_6H_5I]_0 = 54.2$  ppm; black solid circles, triacetylene,  $[C_6H_5I]_0 = 52.9$  ppm,  $[C_2H_2]_0 = 526.3$  ppm; red solid triangles, diacetylene,  $[C_6H_5I]_0 = 52.9$  ppm,  $[C_2H_2]_0 = 526.3$  ppm.

shows the comparison between the diacetylene and the triacetylene profiles for experiments conducted at nominal pressure of 25 atm with and without acetylene in the initial mixture. Clearly the presence of acetylene enhances the formation of the polyacetylenes supporting the hypothesis that the polymerization process plays a key role at high temperatures. In addition we can also notice that the profiles in Figure 31 start increasing all in the same temperature range (around 1400–1450 K) which suggests that the mechanistic pathways are common for the two cases presented.

The experimental results as well as the modeling profiles for both diacetylene and triacetylene are shown in Figures 32 and 49 (Supporting Information). The most evident discrepancy

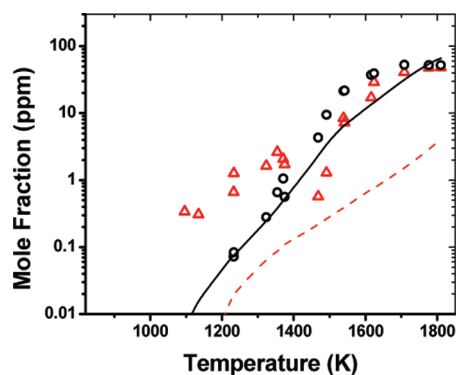


**Figure 32.** Black circles, diacetylene experiments; black line, diacetylene simulation; red triangles, triacetylene experiments; red dashed line, triacetylene simulation.  $[C_6H_5I]_0 = 58.1$  ppm,  $[C_2H_2]_0 = 236.3$  ppm,  $p \approx 50$  atm.

consists in the substantial underestimation of the profiles for triacetylene. As also pointed out in the first part of the article in relation to the results presented in Figure 23, the polymerization process responsible for the formation of triacetylene is clearly not described accurately by the model. On the other hand, we can notice that the triacetylene profiles show an early small increase between 1200 and 1400 K where the concentration of diacetylene is nearly zero. This could suggest that other pathways to the formation of triacetylene exist which do not involve the intermediate formation of diacetylene. Further studies are required to improve the accuracy of the mechanisms involved in the formation of diacetylene and triacetylene at high temperatures.

**3.2.7. Effects of Acetone Impurity.** Although the purity of the acetylene as stated by the supplier companies is 99.6% the relative level of acetone, used as a stabilizer for acetylene, can vary typically in the range between 1% and 2% when acetylene is withdrawn from the tank. Several studies have indicated that the acetone impurity does not affect significantly the experimental results on acetylene pyrolysis and oxidation<sup>89</sup> especially when small concentrations of acetylene are utilized. When acetylene is part of a multi-component reactant mixture for studies on acetylene addition reactions such as in the present investigation the consequences of the acetone impurity are expected to be even less relevant since the chemistry is driven by the reactions with the most abundance among the components, i.e., acetylene. For this reason, in this kind of studies acetylene is usually not purified. However with the use of a Balston filter, small mole fractions of acetone were detected in the reactant mixtures and analyzed together with the relative products to estimate the actual magnitude of the uncertainty caused by the presence of such impurity.

First, a sub-mechanism for acetone chemistry was added to the chemical kinetic model. The sub-mechanism is based on the chemical kinetic mechanism used by Colket et al.<sup>90</sup> to accurately simulate experiments on acetylene pyrolysis in the presence of trace amounts of acetone. The reaction rate constants for the decomposition of acetone were updated based on the mechanism proposed by Dooley et al.<sup>91</sup> for the simulation of *n*-decane/iso-octane/toluene surrogate mixtures. The only modification in the rate constants is related to the H-abstraction reaction between acetone and H for which the estimated pre-exponential factor was multiplied by a factor of 2 in order to obtain a better agreement between experiments and simulations. Additional reactions relevant for the acetone

chemistry include the reaction between acetone and phenyl radical studied by Choi et al.<sup>92</sup> and the reaction between  $CH_3$  and HI to form  $CH_4$  and I. The rate constant for the latter reaction was estimated on the basis of the low-temperature work by Seetula et al.<sup>93</sup>

The experimental and modeling results for acetone and the major related products, i.e., methane and toluene, are presented in Figures 33 and 50 (Supporting Information) for the sets

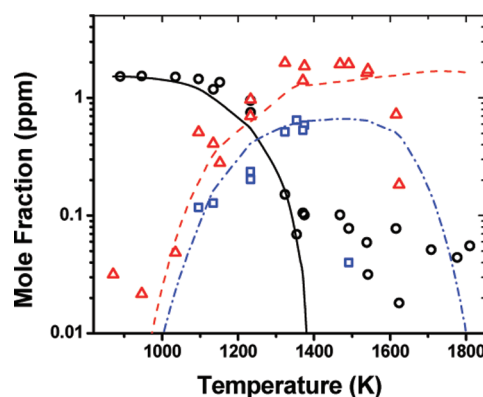


**Figure 33.** Black circles, acetone experiments; black line, acetone simulation; red triangles, methane experiments; red dashed line, methane simulation; blue squares, toluene experiments; blue dash-dotted line, toluene simulation.  $[C_6H_5I]_0 = 58.1$  ppm,  $[C_2H_2]_0 = 236.3$  ppm,  $p \approx 50$  atm.

conducted at 50 atm. The decay of acetone and the formation of the intermediates are quite well reproduced by the model, although at high temperatures methane mole fractions are overestimated. For the purpose of the present study no additional improvements are necessary since the model can already provide a good estimate of how the major stable products of the phenyl + acetylene reaction are affected by the acetone impurity. The comparison between the simulations conducted without and with acetone in the initial reactant mixture is shown in Figures 34 and 51 (Supporting Information) for the compounds which are mostly affected by the impurity. Panels a, b, and c of Figure 34 contain the profiles respectively for single-ring, C12, and C14 compounds for the experimental set conducted with an initial acetylene mole fraction equal to 236.3 ppm. The results clearly indicate that in this case the acetone impurity, around 1.5 ppm, does not significantly influence the formation of the intermediate compounds. The maximum error is around 2–4%. The error in the profiles of the species not shown, which include phenyl iodide, acetylene, and the polyacetylenes, is even smaller.

The analyses performed on the experimental sets conducted with around 500 ppm initial acetylene mole fraction indicate the presence of larger relative amounts of acetone, around 1% of the acetylene in the mixture. As shown in Figure 51d–f (Supporting Information), the effects of the acetone impurity in the profiles are larger than in the previous case but still below the uncertainty in the experimental measurements. The profiles for phenyl iodide, acetylene, and the polyacetylenes are almost unaltered by the presence of acetone. Thus, we can conclude that the acetone impurity does not influence significantly the experimental profiles for the intermediate measured in the present work especially in relation to the experiments conducted with smaller amounts of initial acetylene in the reactant mixture.

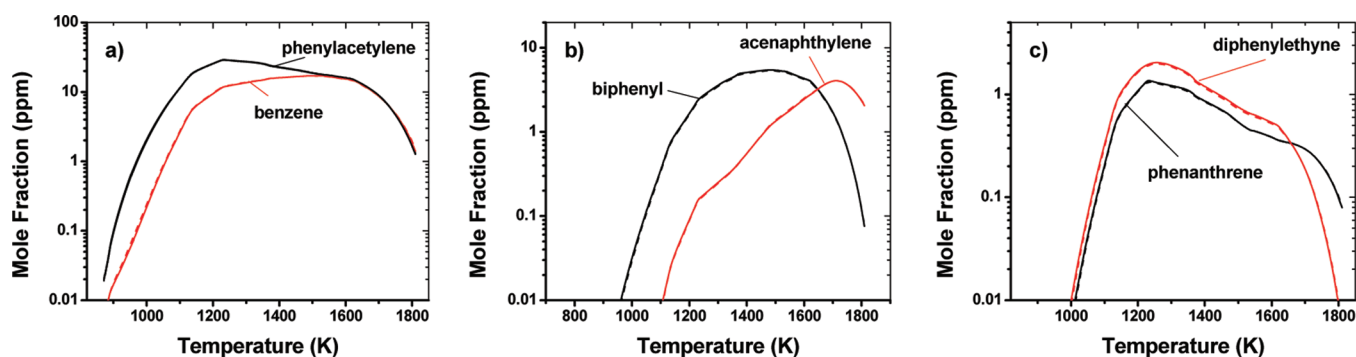


**Figure 34.** Numerical simulations: solid lines,  $[C_6H_5I]_0 = 58.1$  ppm,  $[C_2H_2]_0 = 236.3$  ppm,  $p \approx 50$  atm; dashed lines,  $[C_6H_5I]_0 = 58.1$  ppm,  $[C_2H_2]_0 = 236.3$  ppm,  $[CH_3COCH_3]_0 = 1.5$  ppm,  $p \approx 50$  atm.

**3.2.8. HACA, Addition between Single-Ring Aromatics, Benzyne Chemistry, and Polymerization.** Summarizing the main results on the experimental and modeling study of the phenyl + acetylene reaction we can state that the formation of multi-ring compounds is influenced by two main mechanisms, the HACA mechanism and the reaction between single-ring aromatics. In particular, the C14 compounds, i.e., phenanthrene and diphenylethyne, derive mainly from the reaction between phenyl radical and phenylacetylene, although especially at higher temperatures the contribution of the  $o$ -C<sub>12</sub>H<sub>9</sub> + C<sub>2</sub>H<sub>2</sub> for the formation of phenanthrene becomes important. Once again we need to remember that the  $o$ -benzyne radical plays a key role in the formation of  $o$ -C<sub>12</sub>H<sub>9</sub> as discussed in the first part of the paper.

With regard to the formation of acenaphthylene the discussion is slightly more complex since the mechanisms involved differ based on the relative concentrations of the phenyl radicals and the acetylene in the system. For low acetylene mole fractions the HACA mechanism is one of the relevant pathways to acenaphthylene although not the dominant. In this case the isomerization of the  $o$ -biphenyl radical is still the most important pathway as in the study on the phenyl pyrolysis. Consequently  $o$ -benzyne becomes a key intermediate in the acenaphthylene formation. When acetylene concentration is increased the HACA mechanism is definitely the main source for acenaphthylene.

As in the phenyl pyrolysis study, above a certain temperature the polymerization process becomes dominant and the PAHs concentrations drop. The temperature range of maximum PAHs production is around 1300–1400 K, after which the experimental profiles for diacetylene and triacetylene rapidly rise. The model does not accurately simulate the chemistry for the polymerization mechanism relevant to high-temperature conditions indicating that additional studies are required to clarify this aspect of the problem. In this case the experimental results suggest that new pathways for the formation of triacetylene could be possible.

## 4. CONCLUSIONS

The pyrolysis of the phenyl radical and the pyrolytic reactions of the phenyl radical with acetylene have been investigated at nominal pressures of 25 and 50 atm and for a temperature range between 900 and 1800 K. The experimental work was performed using GC/GC-MS diagnostic coupled to a high-pressure shock tube apparatus. For the first time it has been possible to detect and accurately measure both small hydrocarbon products including single-ring aromatics and a variety of

multi-ring PAH compounds for which mole fraction profiles have been obtained as a function of temperature. A chemical kinetic model has been developed to simulate the experimental results with particular attention to the formation of the PAH products from both reaction systems. The study helped clarify some of the aspects related to the chemistry involved in the formation of large multi-ring compounds.

In particular, the experimental and modeling results on the phenyl radical pyrolysis indicate that the formation of the PAH compounds is strongly influenced by the benzyne chemistry and especially by the reactions involving the  $o$ -benzyne radical. Such reactions have been proposed as relevant for the production of several multi-ring compounds including the terphenyls, acenaphthylene, and the four-ring species. With regards to the acenaphthylene formation a new reaction rate constant expression for the isomerization between cyclopenta-[a]indene and acenaphthylene was derived from the experimental profiles, while a new reaction pathway for the isomerization of biphenylene was investigated from a theoretical point of view using ab initio calculations. In addition, based on the experimental results, we revealed the importance of several other reactions such as the reaction between phenyl radical and hydrogen iodide and the reaction between phenyl iodide and phenyl radical to form the iodobiphenyls. Similar reactions should be included in future studies on the phenyl radical derived from phenyl iodide.

The investigation on the phenyl + acetylene system revealed that the formation of PAH compounds is driven by the reaction between phenyl radical and phenylacetylene with regard to phenanthrene and diphenylethyne, while the HACA mechanism plays a key role in the formation of acenaphthylene when high concentrations of acetylene are present in the reactant mixture.

Finally, both experimental studies suggest that above a certain temperature the polymerization process becomes dominant. Additional theoretical studies are required in order to clarify the relative high-temperature chemistry. The experimental profiles obtained in this work represent a valuable benchmark for the validation of such future studies.

## ■ ASSOCIATED CONTENT

### § Supporting Information

Complete refs 29, 30, 32, 34, and 40; chemical kinetic model, thermodynamic properties, and sensitivity analyses for the major products; experimental and modeling profiles for the data sets not presented in the article. Included for each data set and for each experimental point are the specific experimental



conditions (temperature, K; pressure, atm; reaction time, ms) and mole fractions of the major products (ppm). Included for each optimized stationary structure are the Cartesian coordinates (Å), uB3LYP/6-311+G(d,p) energies (hartrees), uCCSD(T)/pp-cVDZ energies (hartrees), and zero-point vibrational energies (ZPVE, hartrees). Also included for the saddle points are the imaginary vibrational frequencies ( $\text{cm}^{-1}$ ). This material is available free of charge via the Internet at <http://pubs.acs.org>.

## AUTHOR INFORMATION

### Corresponding Author

\*E-mail: [kenbrez@uic.edu](mailto:kenbrez@uic.edu)

### Notes

The authors declare no competing financial interest.

## ACKNOWLEDGMENTS

This work was funded by Strategic Environmental Research and Development Program through grant no. WP-1575. The research was also supported in part by the National Science Foundation through TeraGrid resources provided by [www.ncsa.illinois.edu](http://www.ncsa.illinois.edu) under grant no. TG-CHE110038. We thank Drs. R. S. Tranter and R. Sivaramakrishnan for helpful advice and discussion. We also thank S. Gudiyella for valuable suggestions on the development of the chemical kinetic model.

## REFERENCES

- (1) Frenklach, M.; Clary, D. W.; Gardiner, W. C.; Stein, S. E. *Proc. Combust. Inst.* **1984**, 20, 887–901.
- (2) Frenklach, M.; Wang, H. *Proc. Combust. Inst.* **1990**, 23, 1559–1566.
- (3) Gordon, A. S.; Smith, S. R.; McNesby, J. R. *Proc. Combust. Inst.* **1959**, 7, 317–324.
- (4) Frenklach, M.; Clary, D. W.; Gardiner, W. C.; Stein, S. E. *Proc. Combust. Inst.* **1986**, 21, 1067–1076.
- (5) Frenklach, M.; Yuan, T.; Ramachandra, M. K. *Energy Fuels* **1988**, 2, 462–480.
- (6) Frenklach, M. *Phys. Chem. Chem. Phys.* **2002**, 4, 2028–2037.
- (7) Marinov, N. M.; Pitz, W. J.; Westbrook, C. K.; Castaldi, M. J.; Senkan, S. M. *Combust. Sci. Technol.* **1996**, 116, 211–287.
- (8) Richter, H.; Grieco, W. J.; Howard, J. B. *Combust. Flame* **1999**, 119, 1–22.
- (9) Howard, J. B. *Proc. Combust. Inst.* **1990**, 23, 1107–1127.
- (10) McKinnon, J. T.; Howard, J. B. *Proc. Combust. Inst.* **1992**, 24, 965–972.
- (11) Hepp, H.; Siegmann, K.; Sattler, K. *Chem. Phys. Lett.* **1995**, 233, 16–22.
- (12) Böhm, H.; Jander, H.; Tanke, D. *Proc. Combust. Inst.* **1998**, 27, 1605–1612.
- (13) Shukla, B.; Koshi, M. *Phys. Chem. Chem. Phys.* **2010**, 12, 2427–2437.
- (14) Shukla, B.; Koshi, M. *Combust. Flame* **2011**, 158, 369–375.
- (15) Heckmann, E.; Hippler, H.; Troe, J. *Proc. Combust. Inst.* **1996**, 26, 543–550.
- (16) Park, J.; Lin, M. C. *J. Phys. Chem. A* **1997**, 101, 14–18.
- (17) Tranter, R. S.; Klippenstein, S. J.; Harding, L. B.; Giri, B. R.; Yang, X.; Kiefer, J. H. *J. Phys. Chem. A* **2010**, 114, 8240–8261.
- (18) Fahr, A.; Stein, S. E. *Proc. Combust. Inst.* **1988**, 22, 1023–1029.
- (19) Yu, T.; Lin, M. C.; Melius, C. F. *Int. J. Chem. Kinet.* **1994**, 26, 1095–1104.
- (20) Wang, H.; Frenklach, M. *J. Phys. Chem.* **1994**, 98, 11465–11489.
- (21) Richter, H.; Mazyar, O. A.; Sumathi, R.; Green, W. H.; Howard, J. B.; Bozzelli, J. W. *J. Phys. Chem. A* **2001**, 105, 1561–1573.
- (22) Tokmakov, I. V.; Lin, M. C. *J. Am. Chem. Soc.* **2003**, 125, 11397–11408.
- (23) Tranter, R. S.; Fulle, D.; Brezinsky, K. *Rev. Sci. Instrum.* **2001**, 72, 3046–3054.
- (24) Tranter, R. S.; Sivaramakrishnan, R.; Srinivasan, N.; Brezinsky, K. *Int. J. Chem. Kinet.* **2001**, 33, 722–731.
- (25) Lifshitz, A.; Shweky, I.; Kiefer, J. H.; Sidhu, S. S. In *Shock Waves*; Proceedings of the 18th International Symposium on Shock Waves, Sendai, Japan, 1991; Takayama, K., Ed.; Springer-Verlag: Berlin, 1992; p 825.
- (26) Tsang, W.; Lifshitz, A. *Int. J. Chem. Kinet.* **1998**, 30, 621–628.
- (27) Saito, K.; Toriyama, Y.; Yokubo, T.; Higashihara, T.; Murakami, I. *Bull. Chem. Soc.* **1980**, 53, 1437–1438.
- (28) Tang, W.; Brezinsky, K. *Int. J. Chem. Kinet.* **2006**, 38, 75–97.
- (29) Kee, R. J.; Rupley, F. M.; Miller, J. A.; Coltrin, M. E.; Grcar, J. F.; Meeks, E.; Moffat, H. K.; Lutz, A. E.; Dixon-Lewis, G.; Smooke, M. D., et al. *CHEMKIN Collection*, 3.6; Reaction Design Inc.: San Diego, CA, 2000.
- (30) Kee, R. J.; Rupley, F. M.; Miller, J. A.; Coltrin, M. E.; Grcar, J. F.; Meeks, E.; Moffat, H. K.; Lutz, A. E.; Dixon-Lewis, G.; Smooke, M. D., et al. *CHEMKIN*, 4.1; Reaction Design: San Diego, CA, 2006.
- (31) Burcat, A.; Ruscic, B. Ideal Gas Thermochemical Database with updates from Active Thermochemical Tables, <ftp://ftp.technion.ac.il/pub/supported/aetdd/thermodynamics>.
- (32) Wang, H.; Dames, E.; Sirjean, B.; Sheen, D. A.; Tangko, R.; Violi, A.; Lai, J. Y. W.; Egolfopoulos, F. N.; Davidson, D. F.; Hanson, R. K., et al. A high-temperature chemical kinetic model of n-alkane (up to n-dodecane), cyclohexane, and methyl-, ethyl-, n-propyl and n-butyl-cyclohexane oxidation at high temperatures, JetSurF version 2.0, September 19, 2010 (<http://melchior.usc.edu/JetSurF/JetSurF2.0>).
- (33) Richter, H.; Granata, S.; Green, W. H.; Howard, J. B. *Proc. Comb. Inst.* **2005**, 30, 1397–1405 (<http://web.mit.edu/anish/www/MITcomb.html>).
- (34) Kee, R. J.; Rupley, F. M.; Miller, J. A.; Coltrin, M. E.; Grcar, J. F.; Meeks, E.; Moffat, H. K.; Lutz, A. E.; Dixon-Lewis, G.; Smooke, M. D., et al. *CHEMKIN Collection*, 3.7.1; Reaction Design, Inc.: San Diego, CA, 2003.
- (35) Sivaramakrishnan, R.; Tranter, R. S.; Brezinsky, K. *J. Phys. Chem. A* **2005**, 109, 1621–1628.
- (36) Becke, A. D. *J. Chem. Phys.* **1993**, 98, 5648–5652.
- (37) Lee, C.; Yang, W.; Parr, R. G. *Phys. Rev. B* **1988**, 37, 785–789.
- (38) Krishnan, R.; Binkley, J. S.; Seeger, R.; Pople, J. A. *J. Chem. Phys.* **1980**, 72, 650–654.
- (39) Godbout, N.; Salahub, D. R.; Andzelm, J.; Wimmer, E. *Can. J. Chem.* **1992**, 70, 560–571.
- (40) Frisch, M. J.; Trucks, G. W.; Schlegel, H. B.; Scuseria, G. E.; Robb, M. A.; Cheeseman, J. R.; Montgomery, J. A., Jr.; Vreven, T.; Kudin, K. N.; Burant, J. C., et al. *Gaussian 03*, revision D.01; Gaussian, Inc.: Wallingford, CT, 2004.
- (41) Robaugh, D.; Tsang, W. *J. Phys. Chem.* **1986**, 90, 5363–5367.
- (42) Kumaran, S. S.; Su, M. C.; Michael, J. V. *Chem. Phys. Lett.* **1997**, 269, 99–106.
- (43) Kominar, R. J.; Krech, M. J.; Price, S. J. *Can. J. Chem.* **1976**, 54, 2981–2984.
- (44) Butler, E. T.; Polanyi, M. *Trans. Faraday Soc.* **1943**, 39, 19–35.
- (45) Moskaleva, L. V.; Madden, L. K.; Lin, M. C. *Phys. Chem. Chem. Phys.* **1999**, 1, 3967–3972.
- (46) Giri, B. R.; Bentz, T.; Hippler, H.; Olzmann, M. *Z. Phys. Chem.* **2009**, 223, 539–549.
- (47) Rodgers, A. S.; Golden, D. M.; Benson, S. W. *J. Am. Chem. Soc.* **1967**, 89, 4578–4583.
- (48) Wang, H.; Frenklach, M. *Combust. Flame* **1997**, 110, 173–221.
- (49) Park, J.; Burova, S.; Rodgers, A. S.; Lin, M. C. *J. Phys. Chem. A* **1999**, 103, 9036–9041.
- (50) Brooks, C. T.; Peacock, S. J.; Reuben, B. G. *J. Chem. Soc., Faraday Trans. 1* **1979**, 75, 652–662.
- (51) Zhang, L.; Cai, J.; Zhang, T.; Qi, F. *Combust. Flame* **2010**, 157, 1686–1697.
- (52) Lifshitz, A.; Tamburu, C.; Dubnikova, F. *J. Phys. Chem. A* **2009**, 113, 10446–10451.

- (53) Richter, H.; Benish, T. G.; Mazyar, O. A.; Green, W. H.; Howard, J. B. *Proc. Combust. Inst.* **2000**, *28*, 2609–2618.
- (54) Shukla, B.; Tsuchiya, K.; Koshi, M. *J. Phys. Chem. A* **2011**, *115*, 5284–5293.
- (55) Brown, R. F. C.; Choi, N.; Coulston, K. J.; Eastwood, F. W.; Wiersum, U. E.; Jennekens, L. W. *Tetrahedron Lett.* **1994**, *35* (25), 4405–4408.
- (56) Brown, R. F. C.; Eastwood, F. W. *Pure Appl. Chem.* **1996**, *68* (2), 261–266.
- (57) Wiersum, U. E.; Jennekens, L. W. *Tetrahedron Lett.* **1993**, *34* (41), 6615–6618.
- (58) Blake, M. E.; Bartlett, K. L.; Jones, M. Jr. *J. Am. Chem. Soc.* **2003**, *125*, 6485–6490.
- (59) Eyring, H. *J. Chem. Phys.* **1935**, *3*, 107–115.
- (60) Evans, M. G.; Polanyi, M. *Trans. Faraday Soc.* **1935**, *31*, 875–894.
- (61) Wigner, E. *Trans. Faraday Soc.* **1938**, *34*, 29–41.
- (62) Shavitt, I. *J. Phys. Chem.* **1959**, *31*, 1359–1367.
- (63) Scott, L. T. *Pure Appl. Chem.* **1996**, *68* (2), 291–300.
- (64) Raghavachari, K.; Trucks, G. W.; Pople, J. A.; Head-Gordon, M. *Chem. Phys. Lett.* **1989**, *157*, 479–483.
- (65) Dunning, T. H. Jr. *J. Chem. Phys.* **1989**, *90*, 1007–1023.
- (66) Comandini, A.; Brezinsky, K. *J. Phys. Chem. A* **2011**, *115*, 5547–5559.
- (67) Poster, D. L.; Schantz, M. M.; Sander, L. C.; Wise, S. A. *Anal. Bioanal. Chem.* **2006**, *386*, 859–881.
- (68) Jacobelli, C.; Perez, G.; Polcaro, C.; Possagno, E.; Bassanelli, R.; Lilla, E. *J. Anal. Appl. Pyrol.* **1983**, *5*, 237–243.
- (69) Friedman, L.; Lindow, D. F. *J. Am. Chem. Soc.* **1968**, *90*, 2324–2328.
- (70) Copeland, P. G.; Dean, R. E.; McNeil, D. J. *Chem. Soc.* **1960**, 1687–1689.
- (71) Fields, E. K.; Meyerson, S. *Chem. Commun.* **1965**, *20*, 474–476.
- (72) Fields, E. K.; Meyerson, S. *J. Org. Chem.* **1966**, *31*, 3307–3309.
- (73) Lindow, D. F.; Friedman, L. *J. Am. Chem. Soc.* **1967**, *89*, 1271–1272.
- (74) Wang, H.; Laskin, A.; Moriarty, N. W.; Frenklach, M. *Proc. Combust. Inst.* **2000**, *28*, 1545–1555.
- (75) Xu, C.; Braun-Unkhoff, M.; Naumann, C.; Frank, P. *Proc. Combust. Inst.* **2007**, *31*, 231.
- (76) Laskin, A.; Lifshitz, A. *Proc. Combust. Inst.* **1996**, *26*, 669–675.
- (77) Wang, H.; Frenklach, M. *Combust. Flame* **1997**, *110*, 173–221.
- (78) Frenklach, M.; Schuetz, C. A.; Ping, J. *Proc. Combust. Inst.* **2005**, *30*, 1389–1396.
- (79) Whitesides, R.; Kollias, A. C.; Domin, D.; Lester, W. A. Jr.; Frenklach, M. *Proc. Combust. Inst.* **2007**, *31*, 539–546.
- (80) Whitesides, R.; Domin, D.; Salomón-Ferrer, R.; Lester, W. A. Jr.; Frenklach, M. *J. Phys. Chem. A* **2008**, *112*, 2125–2130.
- (81) Gao, Y.; Fessel, K.; McLeod, C.; Marshall, P. *Chem. Phys. Lett.* **2008**, *451*, 8–13.
- (82) Colket, M. B.; Seery, D. J. *Proc. Comb. Inst.* **1994**, *25*, 883–891.
- (83) Appel, J.; Bockhorn, H.; Frenklach, M. *Combust. Flame* **2000**, *121*, 122–136.
- (84) Aguilera-Iparraguirre, J.; Klopfer, W. *J. Chem. Theory Comput.* **2007**, *3*, 139–145.
- (85) Hertzler, J.; Frank, P. *Ber. Bunsenges. Phys. Chem.* **1992**, *96*, 1333–1338.
- (86) Kislov, V. V.; Islamova, N. I.; Kolker, A. M.; Lin, S. H.; Mebel, A. M. *J. Chem. Theory Comput.* **2005**, *1*, 908–924.
- (87) Moriarty, N. W.; Brown, N. J.; Frenklach, M. *J. Phys. Chem. A* **1999**, *103*, 7127–7135.
- (88) Frenklach, M.; Moriarty, N. W.; Brown, N. J. *Proc. Combust. Inst.* **1998**, *27*, 1655–1661.
- (89) (a) Kruse, T.; Roth, P. *J. Phys. Chem. A* **1997**, *101*, 2138–2146.  
(b) Kern, R. D.; Xie, K.; Chen, H.; Kiefer, J. H. *Proc. Combust. Inst.* **1990**, *23*, 69–75. (c) Frank, P.; Just, T. *Combust. Flame* **1980**, *38*, 231–248.
- (90) Colket, M. B. III; Seery, D. J.; Palmer, H. B. *Combust. Flame* **1989**, *75*, 343–366.
- (91) Dooley, S.; Won, S. H.; Chaos, M.; Heyne, J.; Ju, Y.; Dryer, F. L.; Kumar, K.; Sung, C. J.; Wang, H.; Oehlschlaeger, M. A.; Santoro, R. J.; Litzinger, T. A. *Combust. Flame* **2010**, *157*, 2333–2339.
- (92) Choi, Y. M.; Park, J.; Lin, M. C. *J. Phys. Chem. A* **2003**, *107*, 7755–7761.
- (93) Seetula, J. A.; Russell, J. J.; Gutman, D. *J. Am. Chem. Soc.* **1990**, *112*, 1347–1353.